SANDIA REPORT

SAND94-8235 • UC–404
Unlimited Release
Printed January 1995

NaK Pool-Boiler Solar Receiver Durability Bench Test, Vol. 2: Metallurgical Analysis

S. H. Goods, R. W. Bradshaw

Prepared by
Sandia National Laboratories
Albuquerque, New Mexico 87185 and Livermore, California 94551
for the United States Department of Energy
under Contract DE-AC04-94AL85000

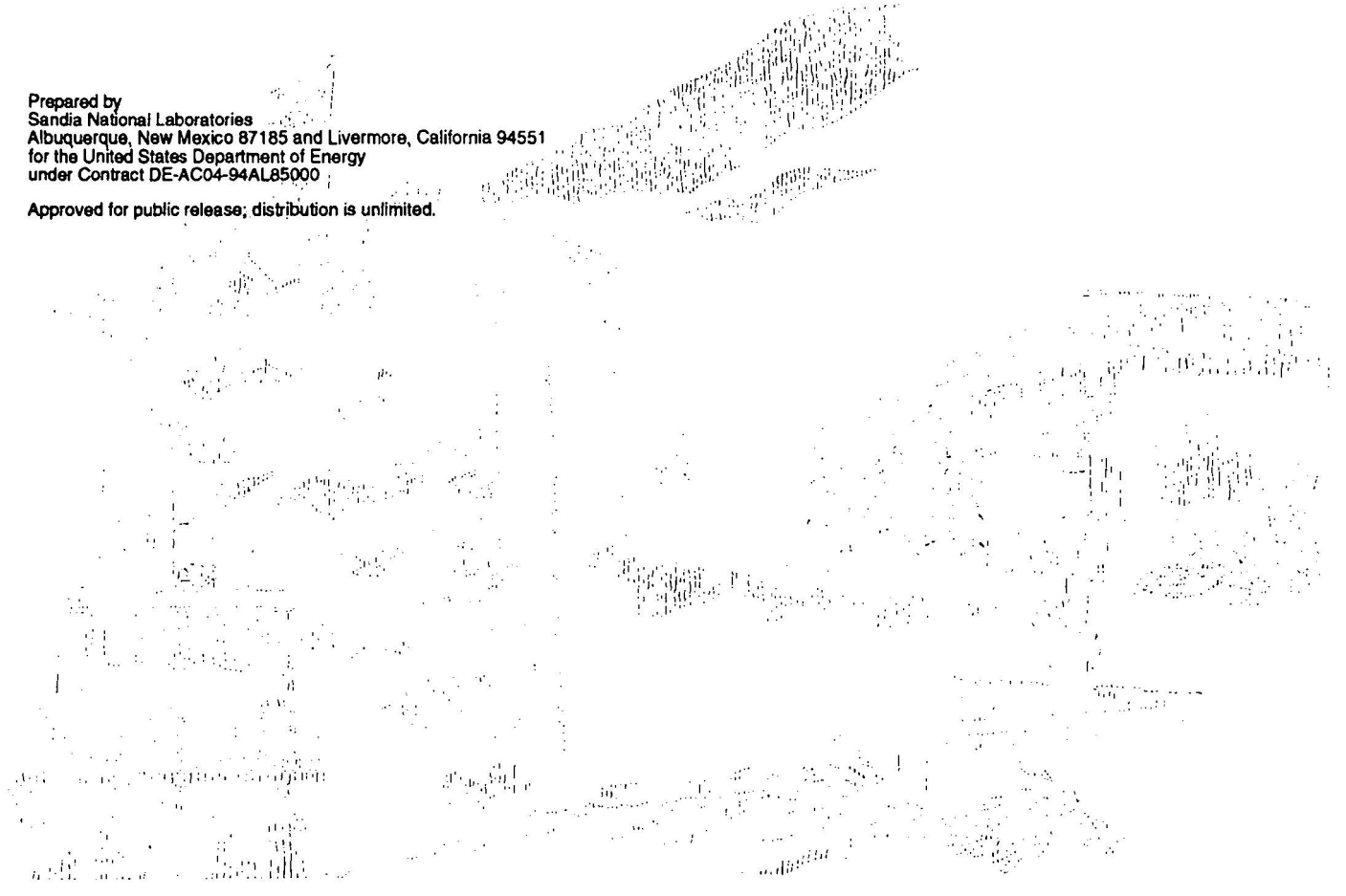

SAND 94-8235 UC-404
Unlimited Release
Printed January 1995

NaK POOL-BOILER SOLAR RECEIVER DURABILITY BENCH TEST, Vol. 2: METALLURGICAL ANALYSIS

S. H. Goods
Engineered Materials and Processes Department

and

R. W. Bradshaw
Materials Synthesis Department
Sandia National Laboratories/California,
Livermore, CA 94550

ABSTRACT

We report on the analysis of the principal materials used in the construction of a NaK-based pool-boiler. The device was operated for 7500 hours and accumulated ≈ 1000 thermal cycles to a peak temperature of 750°C. Haynes 230, a Ni-Cr-W alloy used to fabricate the pool-boiler vessel was found to perform satisfactorily. Air-side corrosion of the pool-boiler vessel was insignificant. The internal surface of the alloy exhibited evidence of some NaK-induced elemental dissolution. This dissolution was somewhat more extensive where the alloy was exposed to the liquid metal compared to regions exposed only to NaK vapor. However, the corresponding metal loss in all regions was inconsequential, never exceeding more than a few microns. Autogenous seam welds of the alloy responded in a similar fashion, exhibiting only minimal metal loss over the course of the experiment. While mechanical property measurements revealed a 50% loss in ductility of the alloy compared to baseline measurements of as-received material, there remained adequate ductility for the anticipated operating environment. An enhanced boiling nucleation surface comprised of stainless steel powder brazed to the vessel ID showed no change in its structure. It remained intact and showed no evidence of cracking after the repeated thermal cycling.

Other materials used in the experiment showed more extensive degradation after exposure to the NaK. IN 600, a Ni-Cr-Fe alloy used to fabricate thermowells, exhibited extensive surface and intergranular dissolution. Grain boundary dissolution was sufficiently severe in one of the thermowells to cause an air leak, resulting in the termination of the experiment. BNi-3, a brazing alloy used to join the pool-boiler vessel, endcaps and thermowells, showed evidence of some dissolution where it was exposed to

the NaK as well as thermal aging effects unrelated to the liquid metal environment. However, all brazes remained structurally sound throughout the experiment. A nickel metal ribbon exhibited evidence of catastrophic dissolution, resulting in the formation of deep (> 30 μm) pits and cavities. A zirconium metal foil used to getter oxygen from the NaK became extremely brittle, the result of the formation of either Zr-oxides or Zr-Ni intermetallic compounds.

TABLE OF CONTENTS

ACKNOWLEDGMENTS

The authors wish to acknowledge a number of individuals for their contributions to this effort. In particular, Andy Gardea (8715) for sample preparation and metallography, Chris Rood (8715), Bernie Bernal (8715) and Nancy Yang (8715) for scanning electron microscopy and microprobe analysis, Dale Boehme (8713) for X-ray diffraction and Ed Soria (8713) for ICP-AES support.

This work supported under DOE Contract #DE-AC04-94AL85000.

NaK POOL-BOILER SOLAR RECEIVER DURABILITY BENCH TEST, Vol. 2: METALLURGICAL ANALYSIS

I. INTRODUCTION

Pool-boiler reflux receivers are being considered for use as the heat transfer interface for parabolic dish/Stirling-cycle engines in remote solar thermal electric generating systems.[1] In the envisioned application, the electric power generating system consists of a parabolic solar concentrator, a cavity receiver and a Stirling heat engine. A tracking system rotates the concentrator allowing the reflected rays of the sun to illuminate the cavity receiver. The receiver is located at the focal point of the parabolic concentrator and receives the focused sunlight on a hemispherical target surface. The function of the cavity receiver (either a pool-boiler or a wicked heat pipe) is to absorb and transfer the thermal energy of the focused sunlight to the Stirling engine. The receiver contains a charge of molten metal (in the present case, a sodium-potassium alloy, NaK-78) which is used as the heat transfer fluid. The thermal energy is transferred from the heated liquid metal to helium gas, the working fluid of a Stirling engine. Figure 1 shows an experimental parabolic dish/pool-boiler receiver located at the National Solar Thermal Test Facility, at Sandia in Albuquerque, NM.

The liquid-metal reflux receiver was conceived as an improvement over direct illumination receivers. In the reflux receiver, the liquid metal is heated and caused to boil by the incident insolation. The resulting vapor is then condensed at the engine heater tubes, supplying its latent heat of vaporization to the helium working gas. The condensate is then returned to the absorber section of the receiver i.e., refluxed. Since it is a two-phase system (liquid-to-vapor), the reflux receiver has the important advantage over directly illuminated heater tubes in that it operates under essentially isothermal conditions. The excellent heat transfer properties of liquid metals also allow for small receivers which minimize capital investment and heat losses.

In order to be cost effective, such a receiver must operate without significant maintenance over its entire lifetime of 30 years or $\geq$ 90,000 hours at maximum temperature. However, the combination of aggressive liquid metal environments, high service temperature, thermal cycling, and thermal gradients inherent to solar receiver applications presents a potentially daunting materials challenge given the extended life requirements. Recognizing this, a series of bench scale experiments was undertaken to assess the durability of the materials used in construction of pool-boiler containers and internal components. This report summarizes the results of a detailed post-mortem analysis of one such pool-boiler experiment that was operated for approximately 7500 hours at 750°C. A companion report addresses, in detail, the motivation of the experiment, the testing methodologies, design, construction and preliminary analysis of the pool-boiler.[2]

I. BACKGROUND

Liquid metal interactions with materials

Liquid metal-induced corrosion is a potential concern in qualifying materials for long duration pool-boiler service. Corrosion by liquid metals can manifest itself in a number

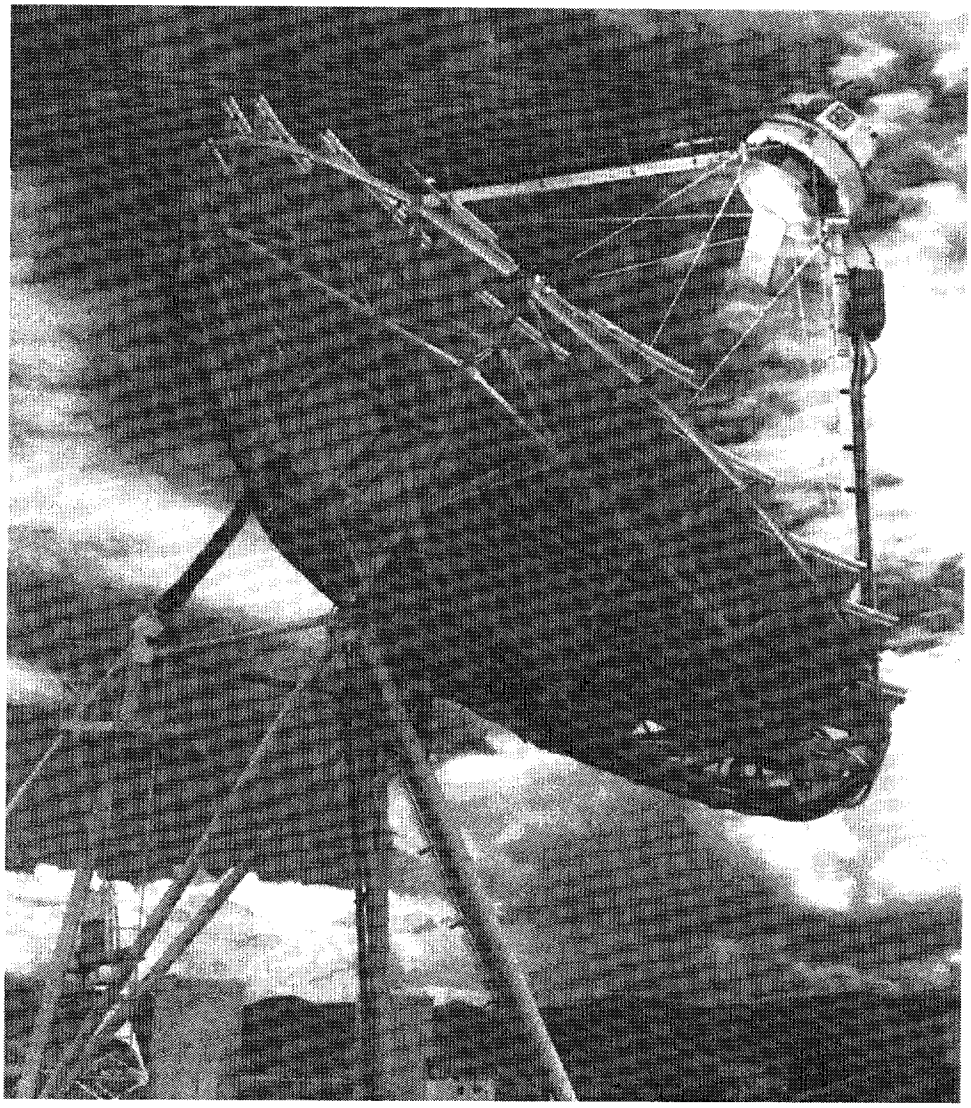

Figure 1. Reflux pool boiler receiver during on-sun testing at the National Solar Test Facility in Albuquerque, NM.

of ways.[3] Dissolution of alloying or interstitial (e.g. carbon) elements in a containment material is the simplest of these corrosion mechanisms as it results directly from the solubility of the elemental constituents of that material in the molten metal. In a closed isothermal system, the degree of dissolution is governed by the equilibrium solubility of a given specie in the liquid metal. In a non-isothermal situation, as is the case for a refluxing receiver, the dissolution behavior is more complex. In regions where the local temperature is higher, the (local) equilibrium concentration of a soluble species will be greater than elsewhere in the liquid pool. Dissolution of that specie into the molten metal will occur. Conversely, in lower temperature regions within the receiver, that dissolved element will be rejected from the liquid phase and either deposit onto internal surfaces or precipitate as a particulate. The net result will be the mass transfer of alloying elements from high temperature regions to low temperature regions of the receiver. Dissolution of the alloying elements may be further exacerbated in a refluxing receiver by the fact that the condensing vapor is essentially solute-free because of the great differences in vapor pressure between sodium and potassium and the metallic elements in the containment alloys. This results in the highest possible concentration gradients and therefore the maximum dissolution rates, even during steady state operation.

Reactions between constituents of containment materials and impurities in the molten metal (such as oxygen) are also often important. For example, oxygen impurities in liquid sodium can increase the dissolution of iron from a containment alloy by promoting the formation of sodium-iron oxide complexes. Alternatively, the interaction of oxygen, sodium and chromium can lead to the formation of sodium chromite, increasing the rate of chromium loss from alloy steels. In the present test, a zirconium oxygen getter was employed to reduce the concentration of residual oxygen. We therefore expect that corrosion of the containment materials by residual oxygen in the NaK was minimal.

Pool-boiler design , materials of construction and operation

The bench scale test vessel, shown schematically in Figure 2 was designed to be heated with a quartz lamp array simulating the fluxes expected during on-sun operation. The principal materials of construction of the pool-boiler were Haynes 230[1], used for the vessel body, fill tubes and end closures, and Inconel 600[2] (IN 600) tubing, used for thermocouple protection tubes (thermowells). The performance of the Haynes alloy was important since it is a likley candidate for the construction of full scale receivers. IN 600 tubing was chosen only because of its availability in the required product form. The compositional specifications of both alloys are shown in Table I.

TABLE I: Compositional specifications of alloys used in pool-boiler (wt.%)

ALLOY	Ni	Cr	W	Fe	Mo	Co	Si	B	P	Mn
Haynes 230	bal	20-24	13-15	3‡	1-3	5‡	0.25-0.75	0.005		0.3-1
Inconel 600	72*	14-17		6-10		*	0.5‡			1‡
BNi-3 braze	bal			0.5			4-5	2.8-3.5		
BNi-7 braze	bal	13-15		0.2			0.1		9.7-10.5	

* Ni + Co = 72%, minimum allowable

‡ Maximum allowable

[1] A registered trademark of of Haynes International, Inc.

[2] A registered trademark of Inco Alloys International, Inc.

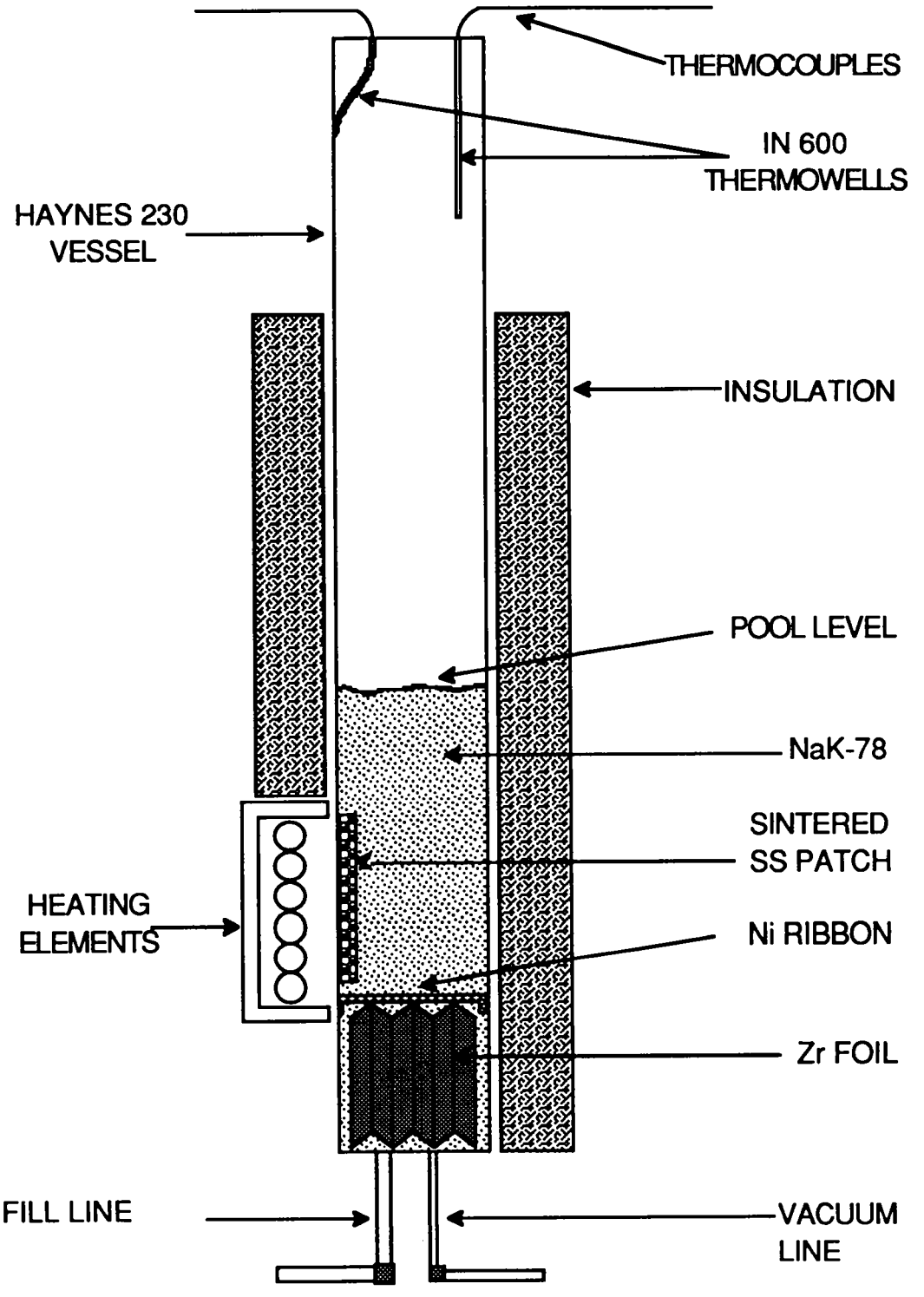

Figure 2. Schematic illustration of the bench-scale pool boiler examined in this study.

Haynes 230 is a nickel-chromium-tungsten alloy that contains small additions of iron, molybdenum, cobalt and silicon. It is a high performance alloy used primarily for elevated-temperature applications and in hostile environments. It has good microstructural stability and as a result, exhibits excellent strength retention and resistance to grain growth after prolonged high-temperature exposure.[4] For the current application, autogenously welded tubing in the solution heat treated condition was used. Solution heated treating for this alloy is performed in air at 1175-1245°C.

The cylindrical vessel was constructed of seam welded Haynes 230 tubing having a wall thickness of 1.25 mm. The pool-boiler was 600 mm long and 45 mm in diameter with Haynes 230 endcaps. These endcaps were brazed to the cylindrical vessel using BNi-3 braze alloy. The braze alloy composition is also shown in Table I. The BNi series of brazing alloys are generally used where corrosion and heat resistance are of primary concern. Many of the braze alloys in this series (including BNi-3) are reported to have "satisfactory" performance for NaK exposure.[5] Vacuum and fill tubes extending out of the bottom of the vessel were also constructed of Haynes 230 tubing and were welded to the endcaps and then back-brazed using the same braze alloy.

Thermowells, made of 3 mm diameter IN 600 tubing, were welded and back-brazed to the endcaps of the pool-boiler vessel. These permitted internal temperature measurements to be made. Inconel 600 is a nickel-chromium-iron alloy that has good resistance to oxidation and caustic corrosion. Its response to prolonged exposure to NaK was unknown. The thermowells were of different lengths allowing for temperature measurement at various locations along the vertical length of the pool-boiler. Several of the thermowells were brazed to the pool-boiler sidewall to allow for the measurement of the vessel temperature. The braze alloy was the same as that used to braze the endcaps to the pool-boiler vessel.

A strip of zirconium sheet measuring 0.1 mm x 25 mm x 100 mm was placed in the bottom of the boiler to getter any residual oxygen in the NaK alloy. The zirconium foil was held in place with a nickel ribbon approximately 3 mm in width and 0.2 mm in thickness. The ribbon was spot welded to the sidewall of the boiler.

The vessel was mounted vertically and filled with 0.34 kg of NaK-78, a eutectic mixture of sodium and potassium that contains 22 wt.% Na and 78 wt.% K. It is liquid between -12.6°C and 785°C at atmospheric pressure. The charge of NaK yielded a liquid column height of ≈270 mm at room temperature. Hereafter, the lower region of the vessel containing the liquid is referred to as the boiler section while the vessel above the liquid surface (and therefore exposed to NaK vapor) is referred to as the condenser. The ratio of the surface area of the pool-boiler vessel to the amount of liquid metal used in this test was close (within about a factor of 2) to that of prospective designs for power generating units. Thus, the present tests should be representative of corrosion effects related to the solvent characteristics of the liquid metal.

Liquid metals and alloys can exhibit significant incipient-boiling superheating. Such behavior manifests itself in the form of large temperature excursions and the inability to maintain constant temperature, even under conditions of constant heat input. Xenon gas at a pressure of about 1/3 torr was added to the NaK vapor space to promote stable boiling.[6] To further promote stable boiling, an enhanced boiling surface consisting of a porous, powder metal (P/M) patch was brazed to the inside of the pool-boiler vessel below the cold liquid level. This P/M patch measured 25 mm x 100 mm and was composed of +60/-80 non-spherical 304L stainless steel powder and was brazed to the vessel ID using BNi-7, a nickel-chromium-phosphorus braze. The patch was fabricated by Friction Coatings Inc. using a proprietary technique. It is important that this enhanced

boiling surface remain effective. Earlier work suggests that boiling characteristics may change with time when surfaces are in contact with a liquid metal.[7] Such changes have been attributed to the reduction of pre-existing oxides on liquid-metal-exposed surfaces after extended operation at temperature, thereby reducing the number of nucleation sites for boiling. The net result was a change in the boiling characteristics during re-heating. In the present case, an additional factor must be considered. Temperature cycling will subject the enhanced boiling surface to thermo-mechanical fatigue due to differential thermal expansion between the stainless steel and the Haynes sidewall. Any cracking, spalling or mechanical failure of the patch could lead to changes in the boiling characteristics of the system with time. Further, similar damage to sintered structures used as wicks for capillary transport of liquid metals in heat pipes would seriously compromise performance. For all of these reasons, the patch was a component of particular interest and was carefully examined.

The pool-boiler was heated from one side with a quartz infrared lamp assembly along a vertical length of the vessel roughly equal to about one-half of the height of the NaK liquid. In order to simulate a diurnal solar cycle, the device was cycled to peak temperature every eight hours. Net time at temperature was approximately 7.5 hours per cycle. The setpoint temperature was 750°C and was governed by a thermocouple reading the pool temperature. The cool-down period was set to 30 minutes which resulted in a minimum pool temperature of approximately 150°C. A tuned PID controller allowed the system to reheat to the setpoint with minimal temperature overshoot or oscillation. Re-heat time was approximately 6.5 minutes. Figure 3 shows the typical temperature/time behavior the pool-boiler system. Although the vessel was only locally heated, gradients in the pool-boiler were quite small; a temperature differential of less than 7°C was measured between the boiler end and the condenser end of the vessel. The constant temperature of both the pool and vapor phase, illustrated by this figure, demonstrates the efficacy of the both the xenon gas and the brazed metal powder patch in promoting stable boiling. A detailed description of the operational characteristics of the pool-boiler is presented elsewhere.[2, 8]

III. RESULTS

Haynes Alloy 230- *As-received material*

The Rockwell hardness of the as-received Haynes 230 alloy was Rb 94. The as-received material had been solution heat-treated in air, which results in the formation of an oxide layer that is subsequently removed by a chemical descaling procedure. This procedure involves immersing the heat-treated tubing in molten hydroxide followed by a nitric and hydrofluoric acid treatment. These aggressive agents can cause some near-surface grain boundary corrosion and cracking. This cracking has no effect on mechanical properties or corrosion resistance.[9]

A second phase microstructure remains after solution heat treatment. This is shown in Figures 4a and b which are scanning electron micrographs (SEM) of a polished and etched cross-section of the as-received alloy. The micrographs reveal that the material contained a relatively uniform distribution of second-phase particles. This "primary" precipitate microstructure in the solution heat treated condition consists of face-centered cubic M_6C particles (as Ni_3W_3C). Chromium or other alloying elements may substitute for nickel in the carbide. These precipitates are stable and do not revert to solution. Extended high temperature exposure results in the formation of "secondary" chromium

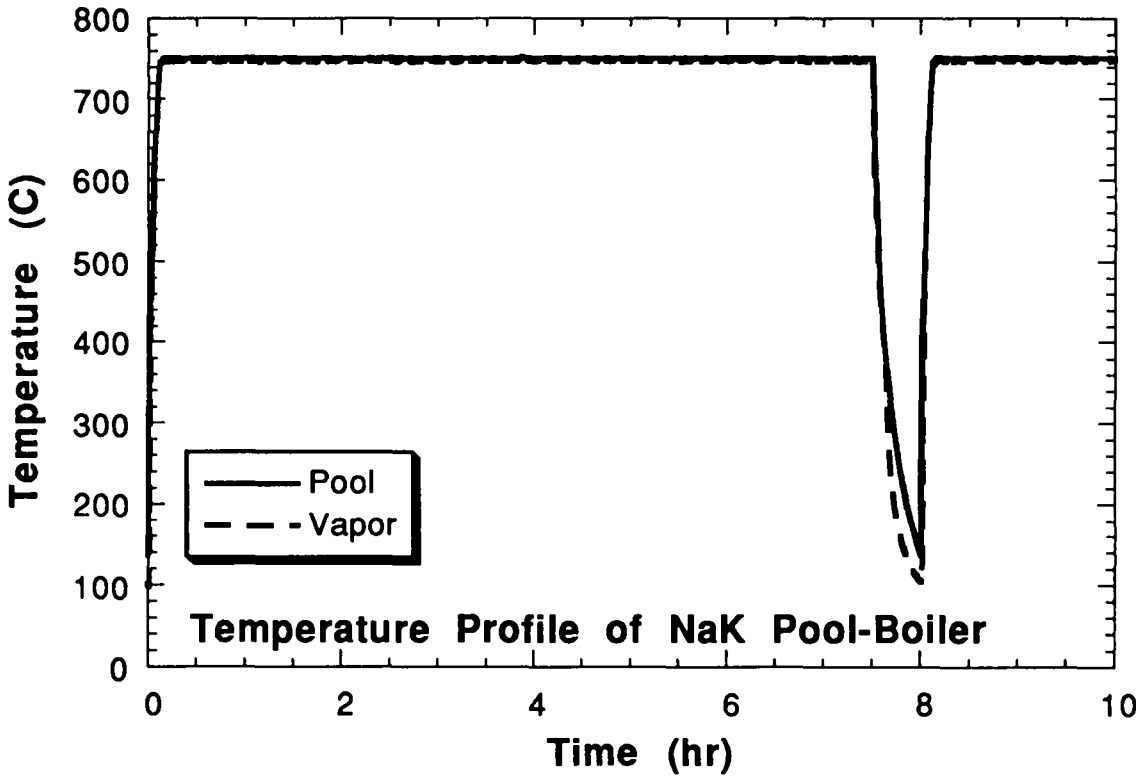

Figure 3. Typical temperature vs. time profile for pool-boiler. 8-hour cycle was continuously repeated to simulate three diurnal cycles for each 24 hours of operation. The temperature stability of the experimental device remained nearly constant with time over the entire duration of the test.

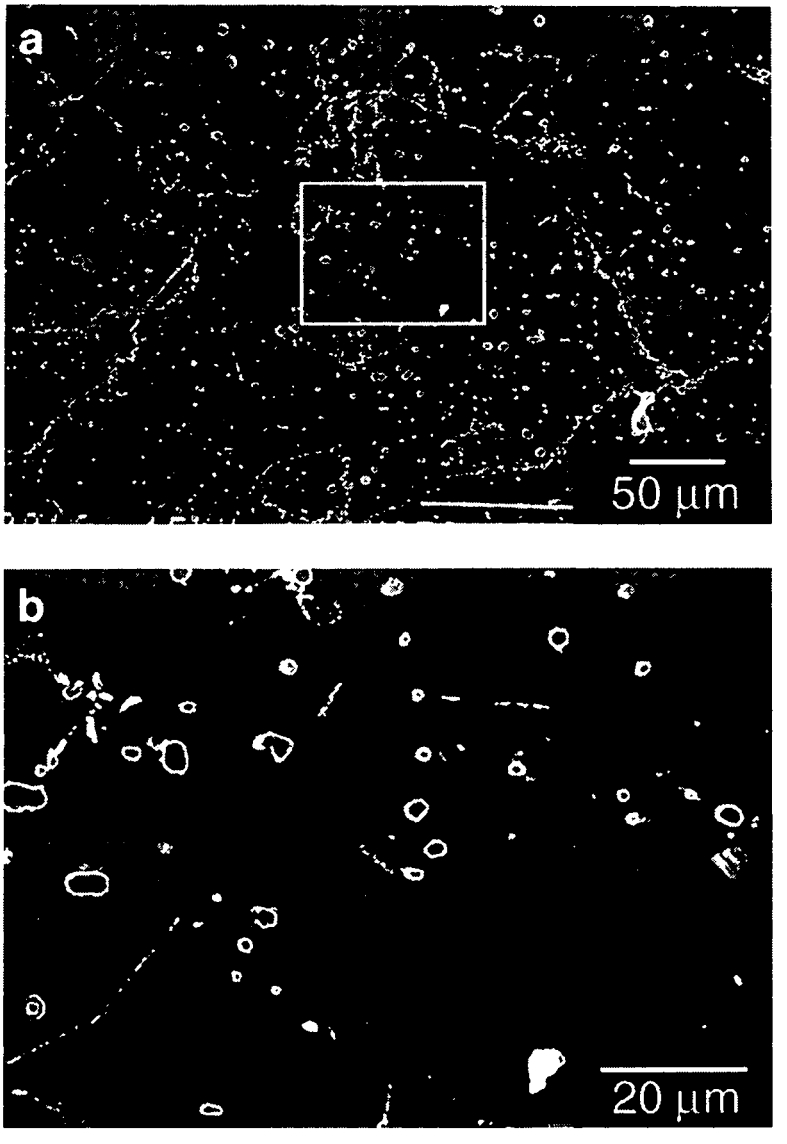

Figure 4. a,b) Scanning electron micrographs of as-received microstructure of solution heat-treated Haynes 230 alloy used in construction of pool-boiler. Solution heat-treated alloy contains tungsten carbide precipitates.

tungsten carbides of the form $M_{23}C_6$. These precipitates have minimal impact on the performance of the alloy.

Energy dispersive spectroscopy (EDS), a semi-quantitative technique, was used to characterize the composition of the alloy and its microstructure. The overall composition of the alloy obtained from an area scan of the as-received tubing is shown in Table II. The results agree favorably with the heat analysis supplied with the tubing. Table II also shows a spot mode analysis of a second phase particle which indicates that these precipitates have an elevated tungsten concentration and an overall composition that is generally consistent with that expected of the precipitate microstructure.

Figures 5a and b are scanning electron micrographs of the ID of the as-received tubing. Marks from the tube forming process are evident in Figure 5a. The particulates and grain boundaries that are shown in Figure 5b are revealed as the result of the chemical descaling procedure. The particulates on the tube surface have essentially the same composition as that indicated in Table II for the second phase particulates.

TABLE II: Elemental analyses of Haynes 230 by EDS (wt.%)

LOCATION	Ni	Cr	W	Fe	Mo	Co
HEAT ANALYSIS	bal	21.96	14.06	1.45	1.26	0.29
AS-RECEIVED (area)	66.75	19.99	10.43	1.01	1.28	0.39
2nd PHASE* (spot)	28.82	15.45	47.73	0.76	6.59	0.00
REGION A	42.71	9.49	41.97	1.66	3.76	0.00
REGION B	64.61	19.03	12.87	2.40	1.10	0.00

*as-received alloy

Haynes Alloy 230 - *pool-boiler vessel*
- NaK-exposed surface

Visual inspection of the pool-boiler surface exposed to boiling NaK for 7500 hours revealed a distinctly "matte" finish unlike the relatively bright finish of the as-received tubing. Scanning electron micrographs of this surface are shown in Figures 6a and b. Figure 6a, a low magnification image, shows a complex surface structure clearly altered from that of the as-received tubing. At higher magnification, Figure 6b reveals that the structure consists of particulates uniformly decorating the surface. As above, EDS analysis was used to assess the composition of these features and the base material to which they are attached. The particulates (indicated in Table II as REGION A) have a composition similar to the second phase particles described in the previous section.

The prominence of these features results from the recession of the alloy matrix. It is reasonable to attribute the recession of the alloy surface to the preferential dissolution of matrix nickel and chromium into the liquid metal pool (relative to the tungsten-rich precipitates). Reliable solubility data for the transition metals and tungsten in liquid NaK are quite limited. Such data as are available for the principal constituents in the alloys studied here are summarized in Figure 7.[10-14] Note that these data concern sodium or potassium as the solvents, rather than NaK. The data in Figure 7 indicate that tungsten should be the most soluble of the principal alloying elements of Haynes 230 at the temperature of the present test, 750°C. These data are contrary to our present observations in that the W-rich precipitates appear to be less soluble than the nickel and

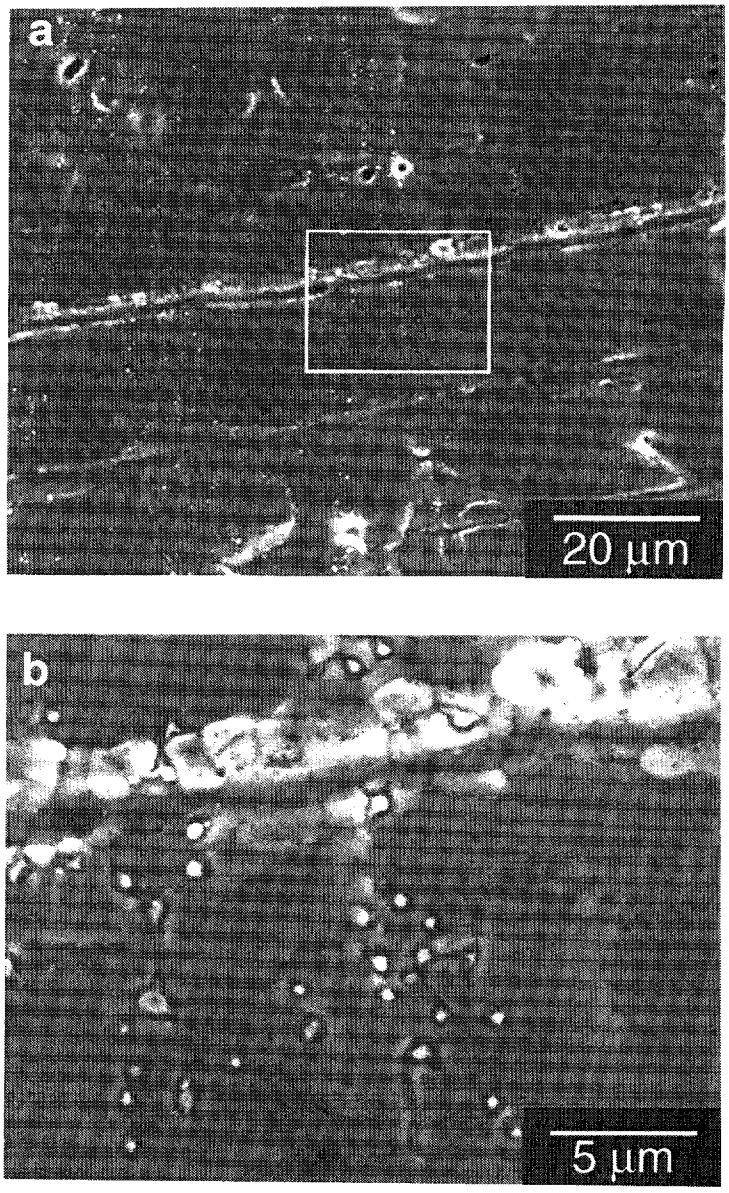

Figure 5. a) Internal surface of as-received Haynes 230 tubing. Parallel striations result from the tube forming process. b) Higher magnification image reveals presence of W-rich precipitates at the tube surface.

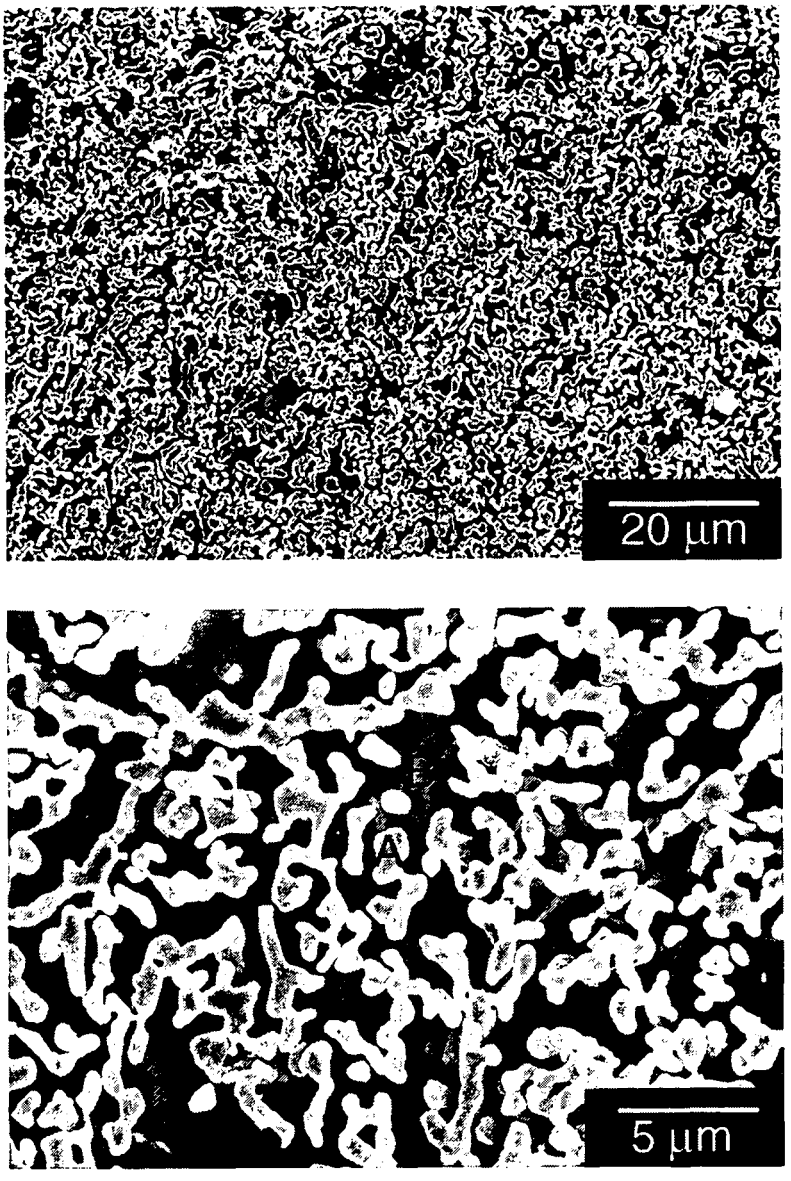

Figure 6. Internal surface of pool-boiler exposed to NaK liquid after 7500 hours at temperature. a) Features on the surface are W-rich precipitates exposed by the recession of the alloy matrix. b) Higher magnification reveals the morphology of the surface structure and the presence of grain boundary dissolution. Regions A and B refer to locations of EDS analysis in Table II.

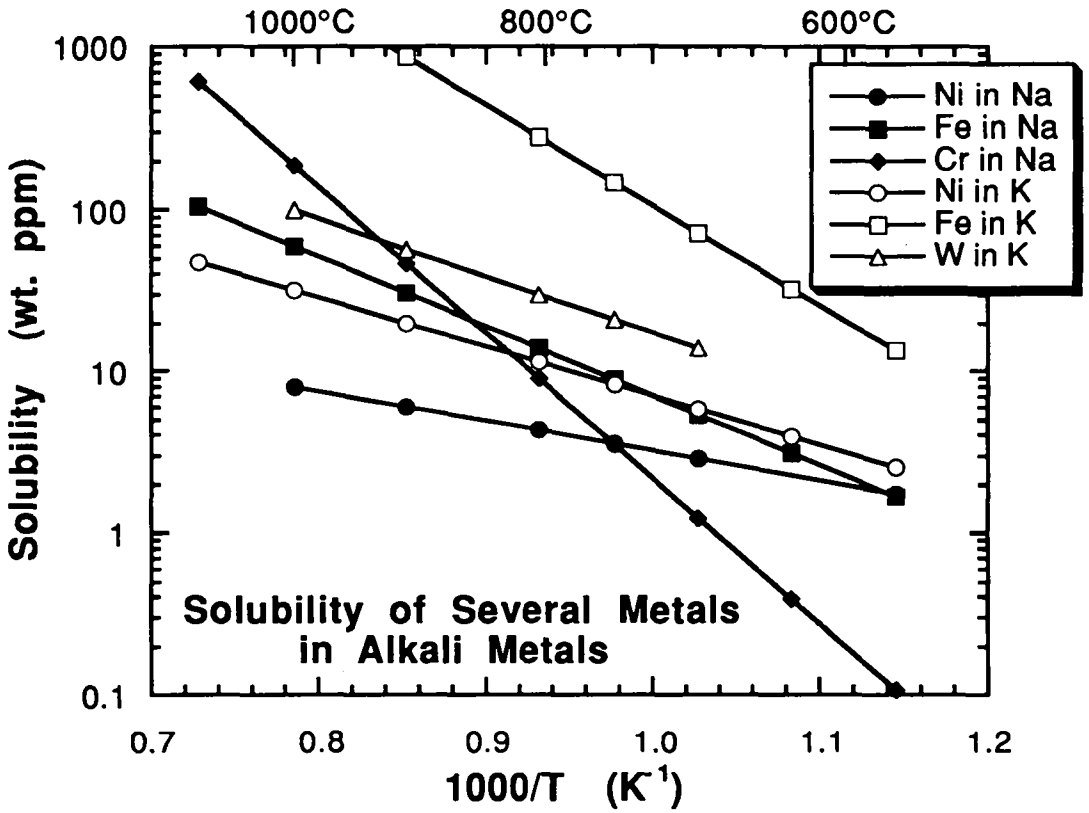

Figure 7. Temperature dependence of the solubility of nickel, iron, chromium and tungsten in sodium and potassium (from Refs. 10-14).

chromium in the matrix. Differences in the behavior of tungsten in the present experiment from that suggested by Figure 7 may be due to differences in the solvent character of NaK versus either sodium or potassium. Additionally, in many of the earlier studies, solubility measurements may have been influenced by oxygen concentrations considerably greater than that in the present experiment. Thus, the applicability of this data in the present case is not clear.

An EDS spot analysis of the alloy surface between the particles (REGION B) is given in Table II. These areas have the general composition of the as-received alloy, which suggests that, within the resolution of the technique, there was no preferential dissolution of the primary alloying constituents (Ni, Cr, W). Recessed grain boundaries can be seen in Figure 6b suggesting that dissolution of the alloy is somewhat more rapid at the grain boundaries than within the grains.

Metallographic cross-sections were prepared from samples of the Haynes alloy cut from the boiler section of the vessel. These specimens were electroplated with copper prior to mounting and polishing in order to preserve the surface structure shown in Figures 6a and b. Figures 8a and b are backscatter electron (BSE) images of one such cross-section that was polished but not etched. Contrast in these BSE images is sensitive to the atomic mass (Z number) of the features being imaged. High-Z regions have higher electron yields and therefore appear brighter than low-Z regions. For example, the upper area in Figure 8a is the copper electroplate which has a lower atomic mass than the average atomic mass of the alloy matrix. Correspondingly, the copper appears darker than the alloy. The alloy matrix near grain boundaries in Figure 8a is somewhat darker than the matrix at the grain interior indicating that the boundaries are slightly depleted in tungsten relative to the matrix. The bright features in Figure 8a are the carbide precipitates which have the highest net atomic mass of any of the features in the alloy (in this work we have not attempted to differentiate between the "primary" M_6C and $M_{23}C_6$ carbides formed by thermal aging). These features decorate the grain boundaries and the interface between the specimen and the copper plating. The precipitates that are arrayed along the interface between the alloy and the plating correspond to the surface structure shown in Figures 6a and b. Figure 8b reveals that the matrix between these precipitates is cusped as a result of its dissolution into the NaK pool. While quantitative measurements of metal loss are not possible, Figures 8a and b suggest that the extent of metal dissolution is small and is likely to be only 3-5 μm. We estimate that the total amount of alloy dissolved from the vessel sidewall is on the order of 1-3 grams.

Examination of the surface morphology of the autogenous seam weld exposed to the NaK indicated no significant differences from the general alloy surface just described. The recession of the alloy matrix and the degree to which the tungsten-rich precipitates decorate the surface in the weld zone are both comparable to that shown for the parent metal in Figures 6 and 8.

– vapor exposed surface

Visual examination of the interior surface of the vessel revealed a distinct "waterline" delineating the pool-boiler from the condensing region. Figures 9a and b are scanning electron micrographs that show the surface of the vessel well above the liquid level. The surface had a morphology intermediate between the as-received material and the surface exposed to liquid NaK. The tungsten-rich particles are less well defined than those shown in the previous figures suggesting that the degree of dissolution of the matrix by the vapor phase was somewhat less extensive. However, the grain boundary etching is more apparent than before simply because the precipitate structure is less well defined and does not mask the grain boundaries. The composition of both the particles and of the underlying matrix are essentially identical to that reported above for the surface

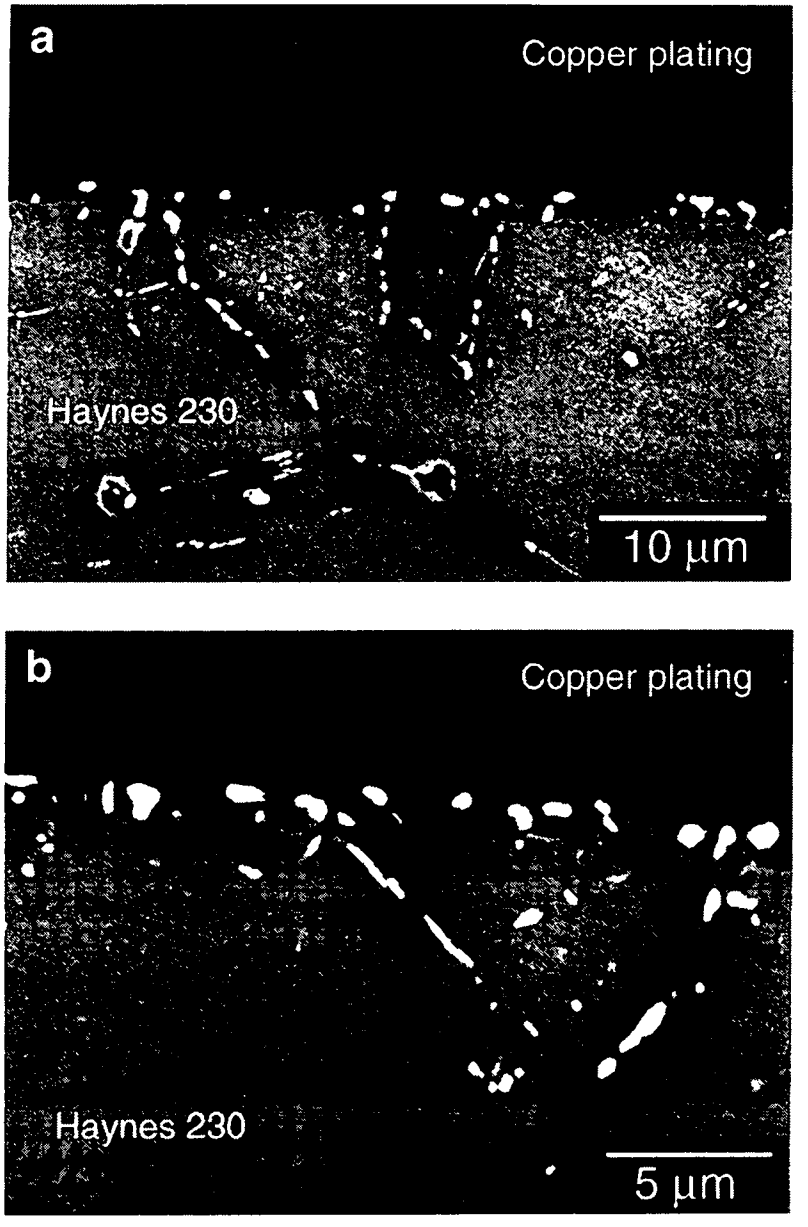

Figure 8. Backscatter electron images of metallographically prepared cross-section of Haynes 230 exposed to NaK liquid. Copper plating was applied prior to sectioning to protect fine surface features. a) Haynes alloy surface is decorated with W-rich precipitates. Grain boundary cavitation is present as the result of the heat treating and surface cleaning procedure. It is not the result of NaK exposure. b) Recession of the alloy matrix from the NaK-exposed surface is evident at higher magnification.

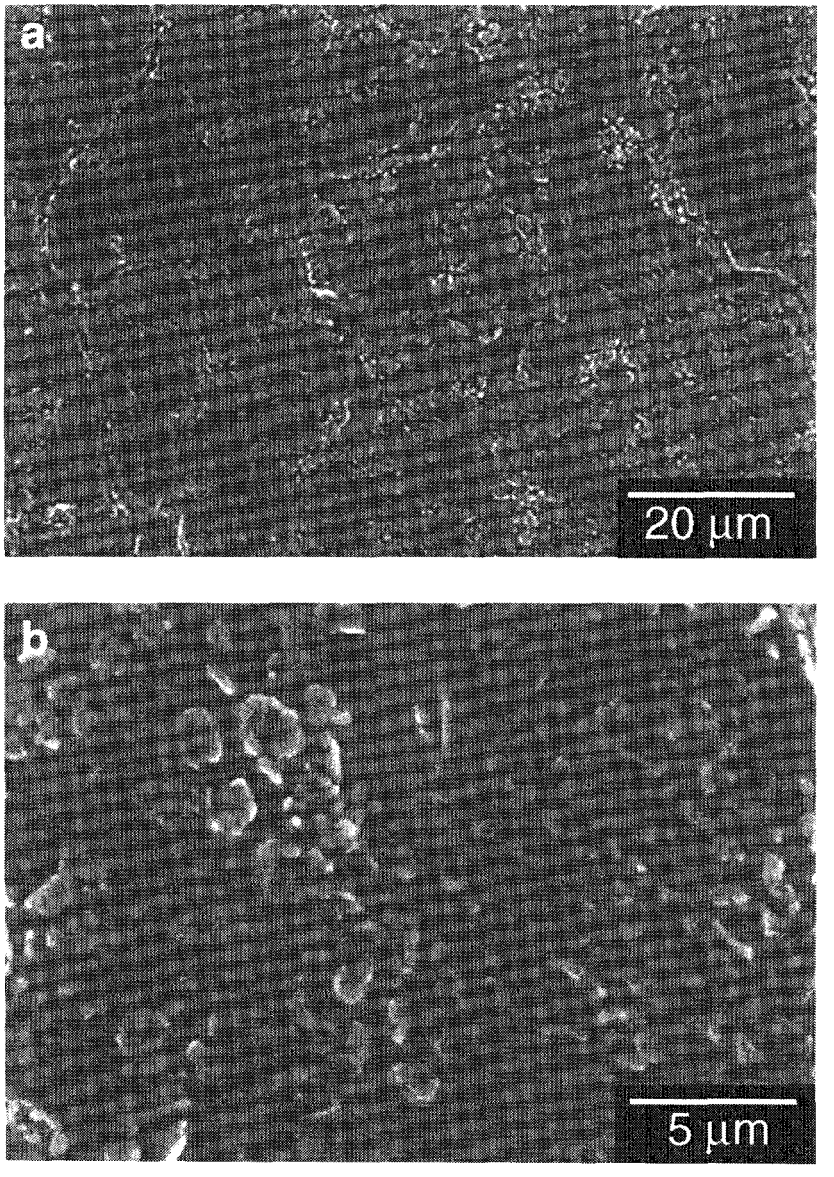

Figure 9. a) Internal surface of pool-boiler exposed to NaK vapor after 7500 hours at temperature. W-rich precipitates are less well pronounced due to less recession of the alloy matrix. Grain boundary dissolution is apparent. b) Higher magnification reveals the morphology of the surface structure.

exposed to liquid NaK. As before, the autogenous seam weld appeared to have been affected to the same extent as the parent alloy in the condenser region.

Dissolution of alloy constituents in the condenser region may differ from that in the boiler section for two reasons. Since the boiling point of potassium is more than 100°C below that of sodium, we expect that the condensate will be considerably richer in potassium than the boiling NaK. Further, unlike the liquid phase, dissolution of the containment material in the condensate is not limited by saturation of dissolved alloy constituents. The NaK condensate is rendered essentially solute-free because the vapor pressures of the alloying elements in the containment materials are negligible compared to those of the alkali metals at these temperatures.

– fill tube

The schematic shown in Figure 3 indicates the presence of a fill tube used to load NaK into the vessel during setup of the experiment. During operation of the pool-boiler, this tube (also Haynes 230) was below the heating elements and uninsulated. Because of this, it was at a considerably lower maximum temperature while the vessel was at its peak temperature during each hold period. It was therefore a likely location for any deposition of dissolved alloy constituents from the boiler or condenser regions. For this reason the interior surface of the fill tube was examined.

Scanning electron micrographs of the tube ID are shown in Figures 10a, b and c. Figure 10a shows the internal surface of the as-received tubing. The grain structure on the ID of the fill tube is revealed as the result of the descaling procedure in the initial processing of the alloy as described in an earlier section. Figure 10b is a similar micrograph taken from the fill tube of the pool-boiler near the lower endcap of the vessel where the temperature was somewhat lower than that of the vessel. The micrograph reveals that while the ID of the NaK-exposed fill line exhibited the identical grain structure, a relatively uniform distribution of discreet particles was observed on the tube ID. EDS analysis of these particles indicated that they contain approximately 50 wt.% W, 30 wt.% Ni, 15 wt.% Cr and smaller concentrations of other elements present in Haynes 230. Thus, the composition of these features strongly suggests that they formed as the result of the deposition of the dissolved constituents of Haynes 230 and IN 600 from the high temperature regions of the pool-boiler vessel. Figure 10c shows the ID of the fill tube further away from the endcap of the pool-boiler vessel where the tube temperature was considerably colder compared to the section shown in Figure 10b. The extent of deposition is much greater in this case than in the previous instance. Again, EDS analysis revealed that the particles were composed of the same elements found in both Haynes 230 and IN 600. Although the absolute amount of material associated with these deposits is very small and is not sufficient to account for the entire amount of material dissolved from the vessel and thermowells, these observations are an indication of elemental mass transport and redeposition driven by the thermal gradients in the pool-boiler.

– mechanical properties

It was important to determine if long-term exposure to NaK resulted in any significant changes to the mechanical properties of Haynes 230. We begin by noting that the alloy exhibits some changes in mechanical properties as the result of prolonged exposure to elevated temperatures, independent of any effects due to the presence of an aggressive environment. The effects of this thermal aging are manifested as a loss in ductility and a change in fracture mode from transgranular to intergranular fracture.[15] In either case, fracture occurs via a process of microvoid growth and coalescence. Table III compares the mechanical properties of as-received material to thermally aged under conditions that closely approximate the conditions experienced by the pool boiler vessel.

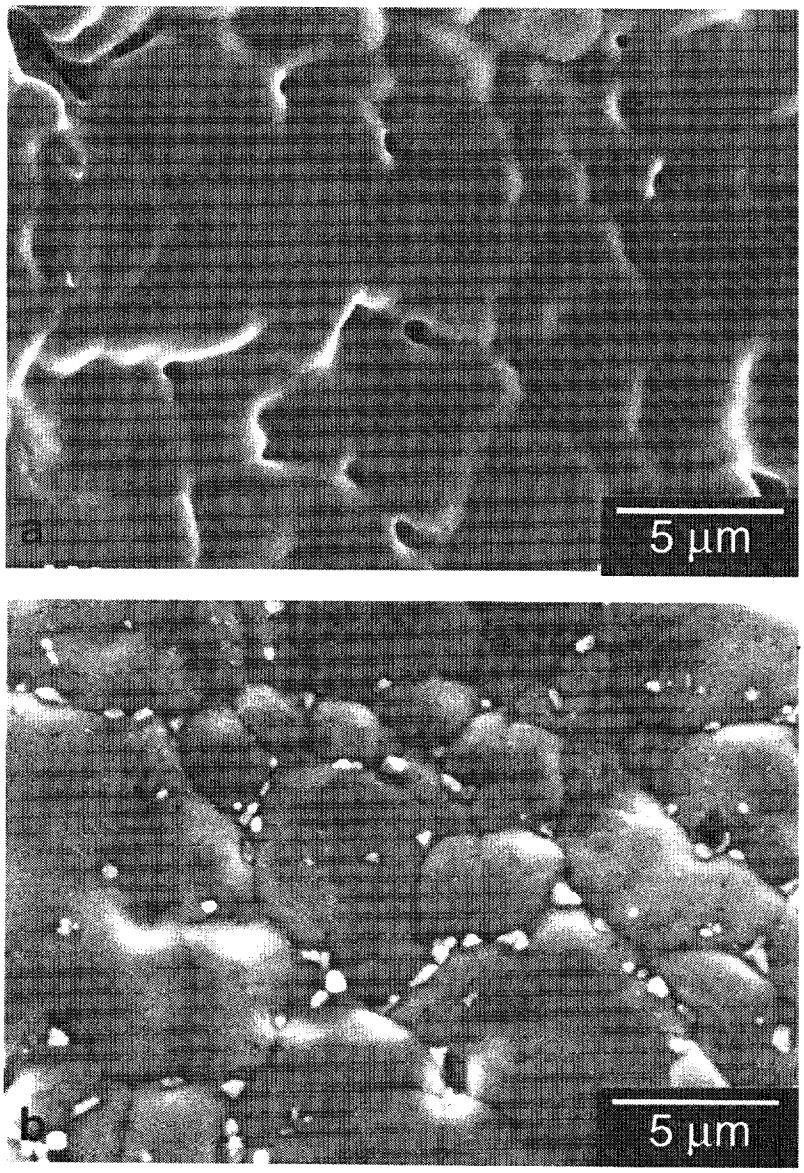

Figure 10. Internal surface of the Haynes 230 fill tubing. a) The grain structure on the ID of the as-received fill tube is revealed as the result of the descaling procedure. b) Deposit is present along the grain boundaries of the fill tube from the pool boiler.

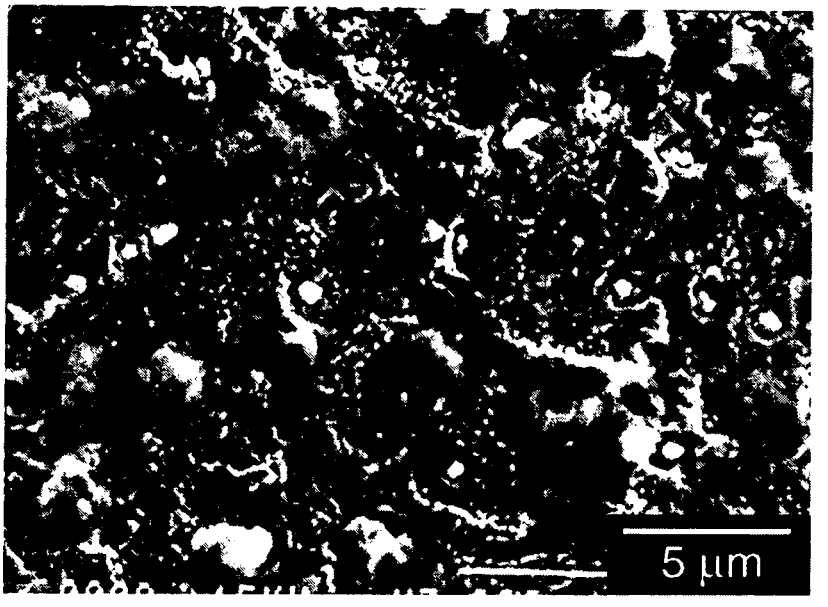

Figure 10. c) ID of fill tubing further away from end cap than that shown in (b). Surface deposition is greater in these colder regions.

Table III: Room temperature mechanical properties of Haynes 230

CONDITION	UTS (MPa)	DUCTILITY (%)	FRACTURE MODE
As-Received	900±5	42±2	Transgranular, ductile
Annealed*	NA	32	Intergranular, ductile
NaK-Exposed (l)	785±60	18±5.5	Intergranular, ductile
NaK-Exposed (v)	800±20	20±1	Intergranular, ductile

* 760°C, 8000 hours, see Reference 15

The Rockwell Hardness of Haynes 230 specimens removed from the pool-boiler after the test was Rb 92 indicating that there was no softening of the alloy as the result of prolonged time at temperature. The mechanical properties of the alloy after exposure to the NaK were directly examined by machining mechanical test specimens from the pool-boiler vessel and comparing the results to those measured for archived sections of the as-received material. Figure 11 compares the typical tensile behavior of a NaK-exposed specimen tested at room temperature to the behavior of the as-received alloy tested under the same conditions. In these tests, the initial strain rate was $2x10^{-4}$ sec^{-1}. In the case of Figure 11, the NaK-exposed specimen was extracted from the boiler section of the vessel. Specimens extracted from the condenser section were also tested and exhibited identical behavior to those exposed to the NaK liquid. The figure shows that the as-received specimens failed at the ultimate tensile strength (UTS) with no necking. In every instance, the specimens cut from the pool-boiler vessel exhibited a measurable ductility loss relative to the as-received alloy. Since Figure 11 shows that work hardening of the alloy was unaffected by NaK (or NaK vapor) exposure, the decrease in the UTS of the specimens extracted from the pool-boiler did not result from as loss in strength, per se, but rather from early fracture of the alloy.

The results of triplicate measurements for specimens machined from each region of the pool-boiler are given in Table III for comparison to the as-received alloy and for Haynes 230 annealed in air at 760°C for 8000 hours.[15] In the table, the specimens extracted from the boiler section of the vessel are denoted as "NaK-Exposed (l)" while those extracted from the condenser section are denoted as "NaK-Exposed (v)". The NaK-exposed specimens exhibited about a 8-15% loss in strength and about a 50% loss in ductility compared to the as-received alloy. Table III also reveals that the loss in ductility is greater than that reported in the literature for the thermally aged alloy. We suspect that the loss in ductility in excess of that reported for air-annealed alloy is the result of the NaK-induced grain boundary dissolution described earlier. Since thermal aging alone results in a change in fracture mode from transgranular to intergranular, the grain boundary dissolution experienced by the NaK-exposed material, although minor in extent, makes the alloy more sensitive to the aging-induced change in fracture mode.

An example of the typical change in fracture mode can be seen in the next two figures. Figures 12a, b and c show the fracture surface of an as-received specimen tested to failure. At low magnification, Figure 12a shows that the fracture surface was quite flat with few distinguishing features. At higher magnification, Figure 12b reveals that the fracture could be described as having occurred via a process of transgranular ductile rupture. Fractured tungsten carbide particles decorate the fracture surface, indicating that these precipitates were well bonded to the matrix. Finally, Figure 12c reveals a generally bi-modal size distribution of dimples, where large, 5-10 μm dimples (nucleated around the fractured carbides) are surrounded by much smaller dimples not associated with

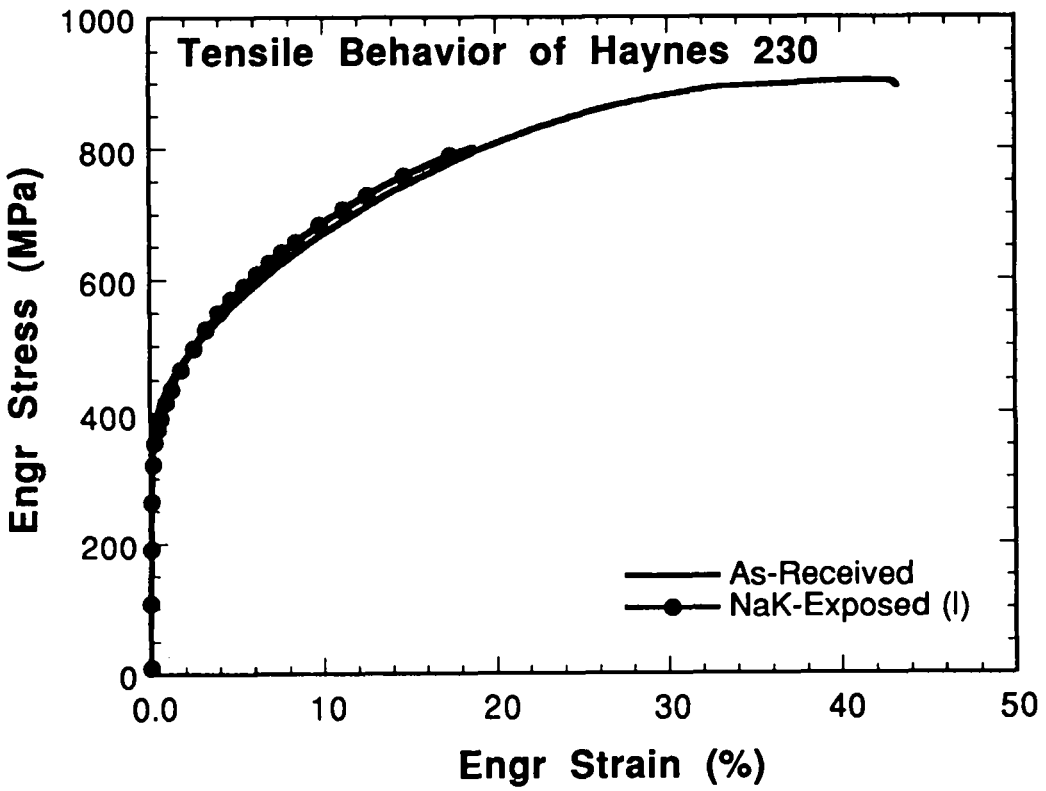

Figure 11. Comparison of uniaxial tensile behavior of as-received Haynes 230 specimen compared to specimen cut from the sidewall of the pool-boiler vessel beneath the liquid level of the NaK. Specimens extracted from the condenser section of the pool-boiler exhibit identical behavior. The data for as-received Haynes 230 presented in Table III was taken from Ref. 15

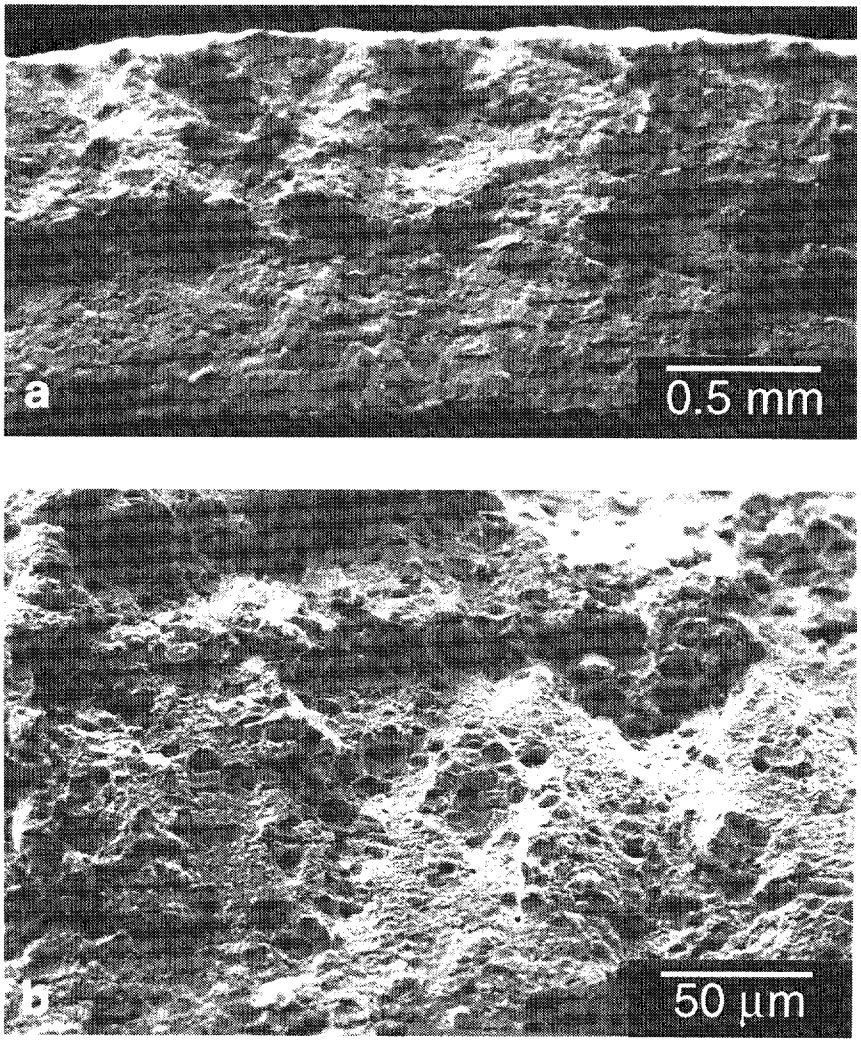

Figure 12. Fracture surface morphology of as-received Haynes 230. a) Fracture surface was quite flat with few distinguishing features. b) Higher magnification image reveals that fracture occurred via a process of transgranular ductile rupture. Fractured tungsten carbide particles decorate the fracture surface, indicating that these precipitates were well bonded to the matrix.

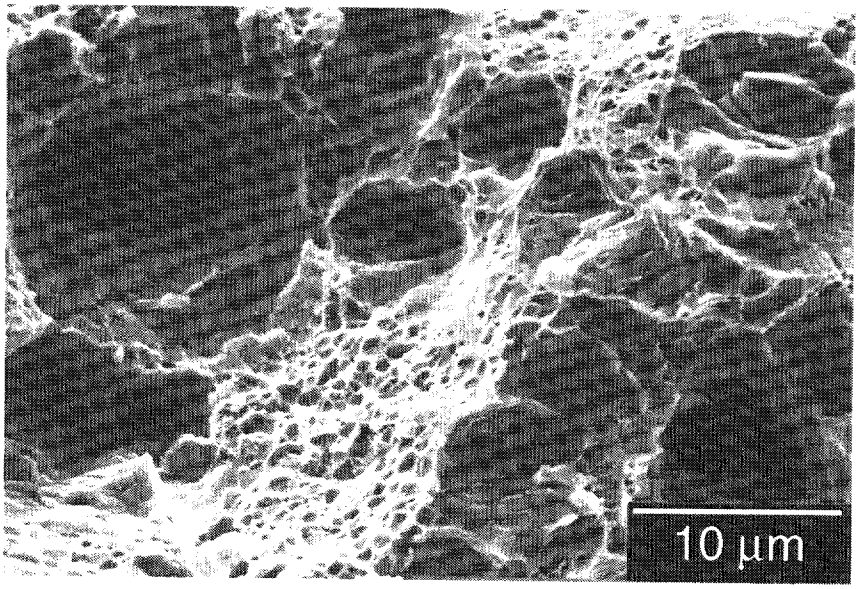

Figure 12. c) Large, 5-10 µm dimples (nucleated around the fractured carbides) are surrounded by much smaller dimples yielding a bi-modal distribution of dimples.

carbides. The fracture surface of the NaK-exposed alloy is shown in Figure 13a. In this instance the fracture surface was intergranular. At higher magnification, Figure 13b reveals that the fracture was still ductile in nature. Figure 13c reveals that the grain boundary facets were decorated with a uniform distribution of dimples with only a few fractured carbides visible.

304L stainless steel powder – *enhanced boiling surface*
Archived sections of the brazed powder structure were used to assess the effects of long-term NaK exposure. Figures 14a, b and c are successively higher magnification SEM micrographs of the as-brazed stainless steel. Figure 14a reveals that the patch was composed of irregularly shaped particles with a free volume previously estimated to be ≈ 60%.[8] The irregular shape of the metal powder particles suggests that they were produced by a water atomization process. After brazing, the particle surfaces are covered with contamination composed of 0.5-2 μm silicon-rich particulates, see Figure 14b. These are likely to be silicon oxide particles. Such contamination is not typical of water atomized metal powders and we suspect that it arises from the post-atomization handling of the powders and/or the brazing process. At very high magnification, Figure 14c reveals the presence of a "terraced" structure on the surface of the metal powder. Such structures can arise from thermal etching.

The brazed patch was examined in detail. There was no evidence of spalling, cracking or any other structural degradation resulting from repeated thermal cycling. This was somewhat surprising in light of the relatively rigorous thermal cycling profile imposed on the patch over the operating history of the pool-boiler. Figures 15a and b are micrographs taken from the brazed patch in the pool-boiler. Figure 15a shows that the patch maintained the same general high surface area, open morphology of the as-brazed patch. The surface contamination shown in Figure 14b and c is no longer apparent. Silica will not be reduced by NaK as the alkali metal oxides are less thermodynamically stable than SiO_2.[16] The absence of the silica contamination is therefore likely the result of some minimal dissolution of the underlying stainless steel allowing the contamination to break free or of thermal cycling which could promote the detachment of weakly bound particles. In addition, the zirconium getter can reduce silica which would facilitate its removal by either loss of adhesion or, possibly, dissolution. Figure 15b shows that the terraced structure on the original stainless steel powder surfaces was no longer visible, suggesting that the stainless steel suffered a very small amount of dissolution due to NaK exposure. This observation supports the argument that the loss of the silica contamination was the result of dissolution of the stainless steel.

The thermal stability of the pool-boiler, as illustrated in Figure 3, remained invariant over the operational history of the device. Thus the small changes in the structure of the metal powder patch, including the loss of the surface contamination, had no impact on its effectiveness to promote reproducible boiling characteristics of the NaK pool. The minimal attack of the stainless steel P/M structure suggests that austenitic stainless steels should not be overlooked as candidate alloys for primary containment vessels when air-side corrosion and strength considerations can be avoided.

Inconel 600 – *thermowell tubing*
Inconel 600 tubing was used to fabricate the thermowells for the pool-boiler vessel. These 3 mm diameter thermowells were located both above and below the NaK liquid level. IN 600 is a nickel-chromium-iron austenitic alloy that has good resistance to oxidation and stress-corrosion cracking. The specified composition for the alloy is given in Table I.

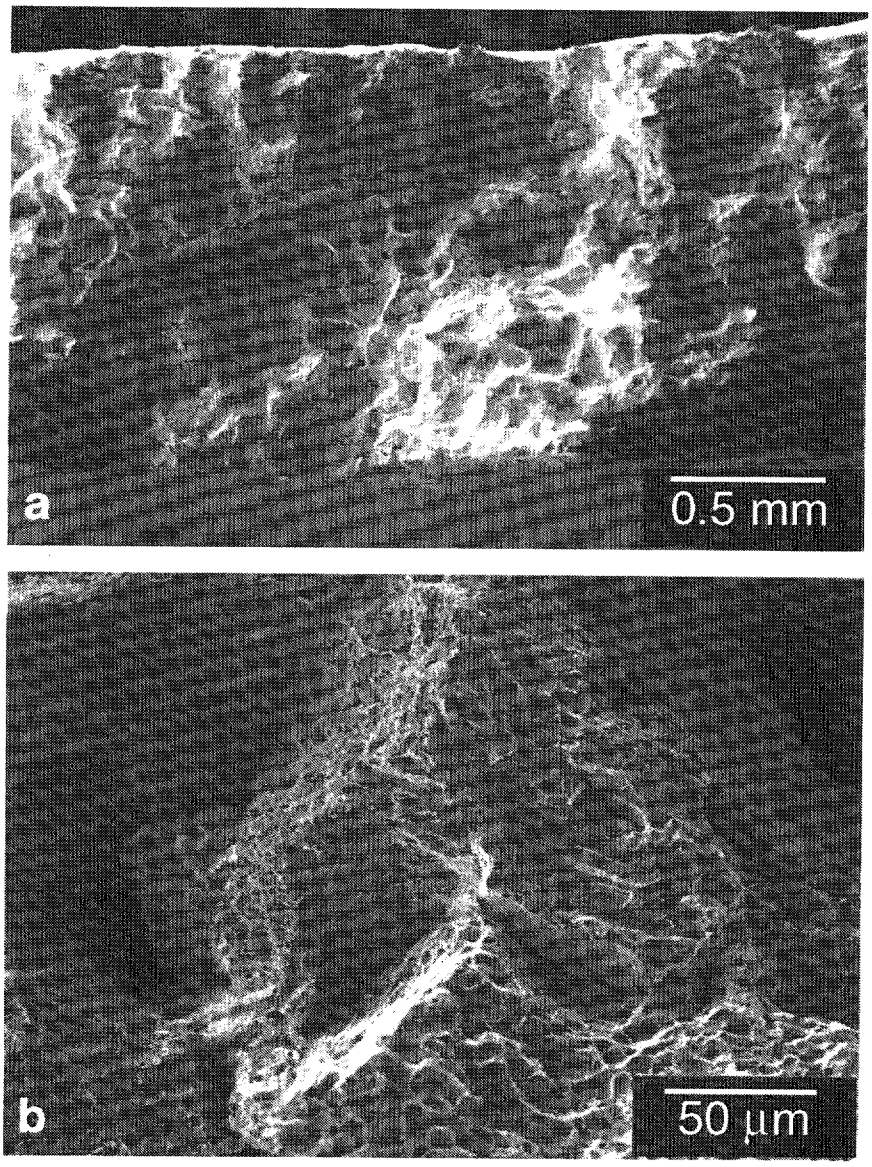

Figure 13. Fracture surface morphology of NaK exposed-Haynes 230. a) Fracture surface is intergranular. b) Grain boundary facets are decorated with dimples indicating that fracture was still ductile.

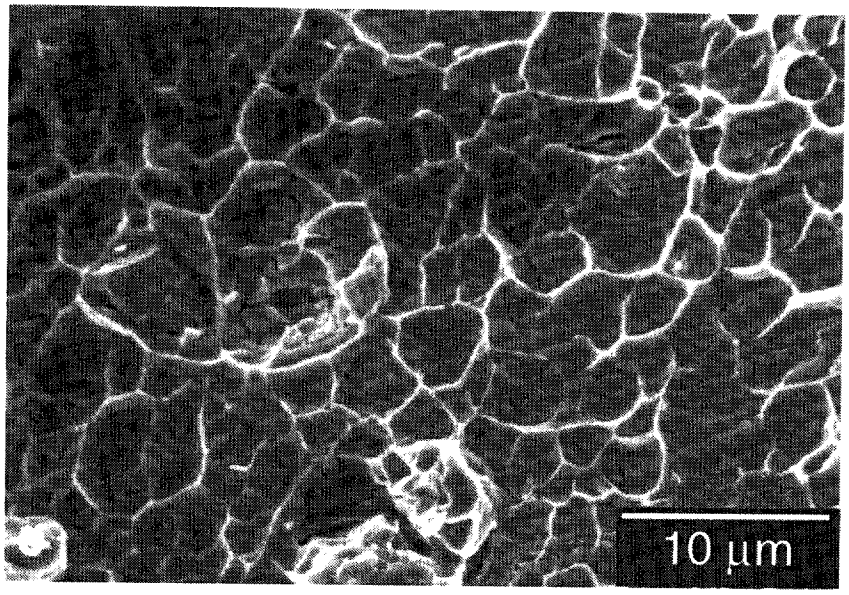

Figure 13. c) Grain boundary facets are decorated with a uniform distribution of dimples with only a few fractured carbides visible.

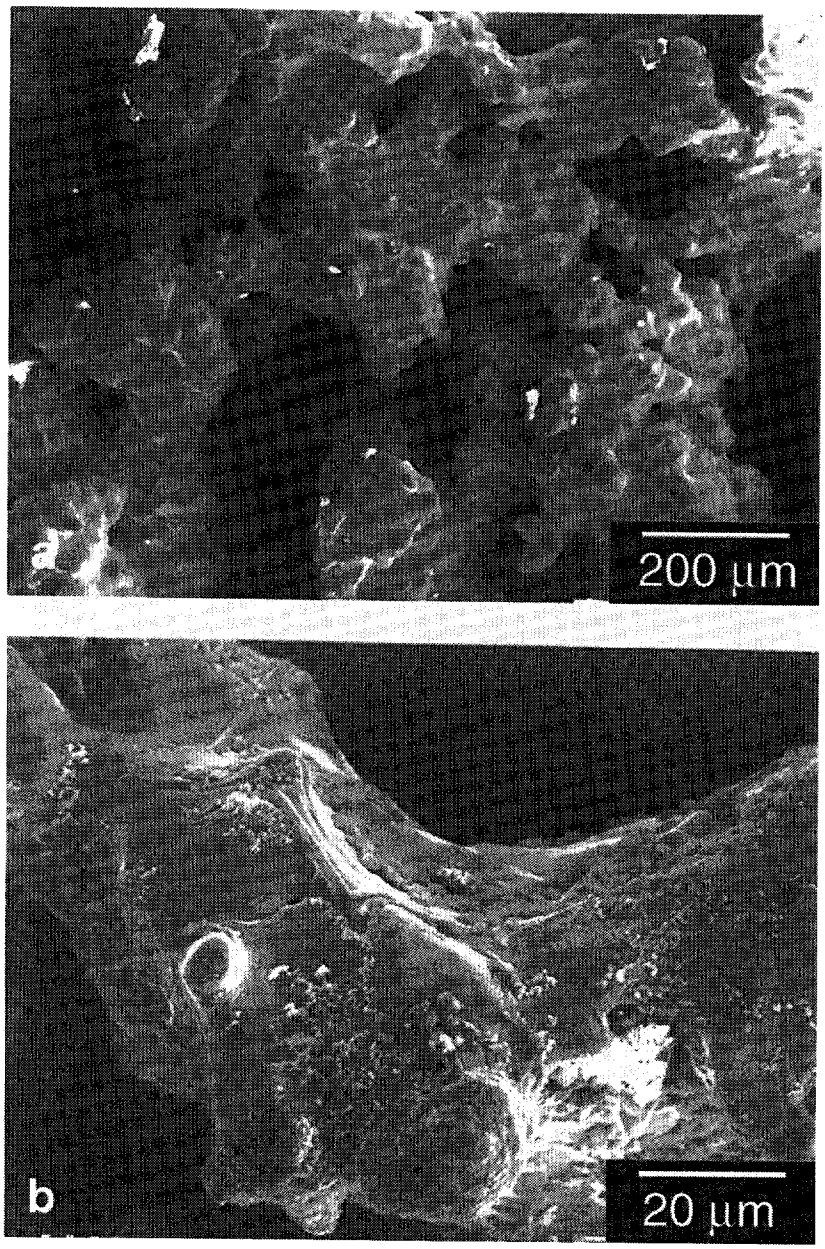

Figure 14. Successively higher magnification micrographs of an as-brazed enhanced boiling surface stainless steel powder patch. a) Irregular stainless steel particles suggest a water atomization process. b) Silica contamination is present on the SS powder particle surfaces.

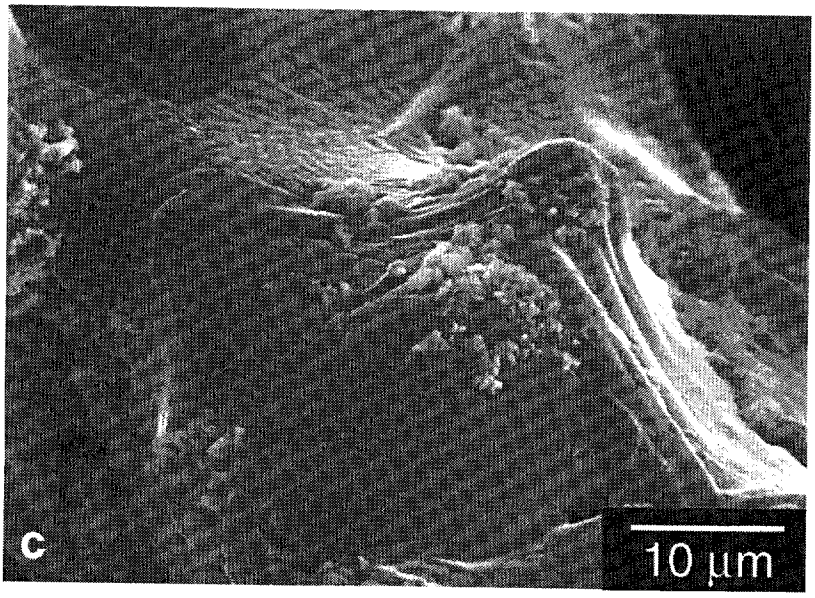

Figure 14 c) Terraced structure on the surface of the metal powder can arise as the result of thermal etching.

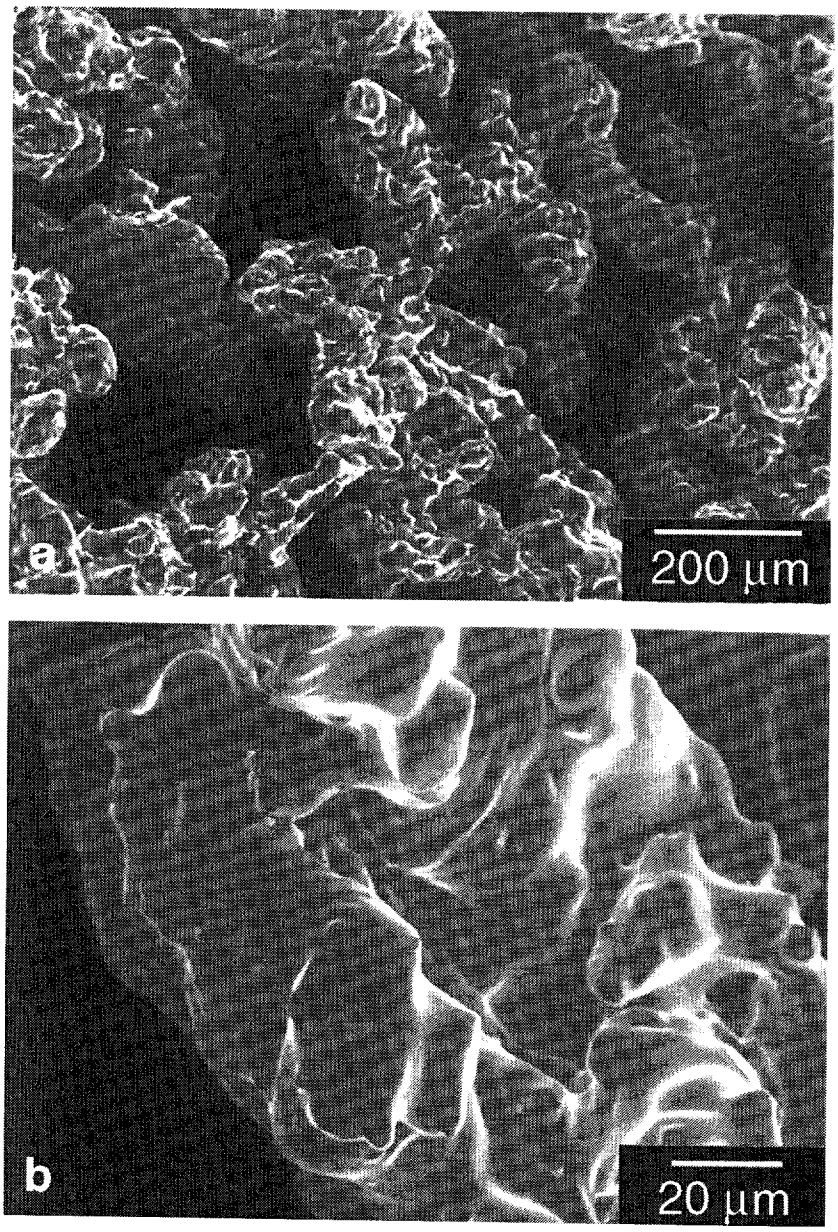

Figure 15. Surface morphology of the NaK-exposed enhanced boiling surface. a) The patch maintained the same general high surface area and open morphology of the as-brazed structure. b) Surface contamination and terraced features are no longer apparent after long-term NaK exposure.

Scanning electron microscopy of the as-received thermowell tubing is shown in Figures 16a and b. Figure 16a shows, at low magnification, a horizontal surface striation and disturbed metal, both indicative of the tube drawing process. Dark regions resulting from surface contamination are also apparent. At higher magnification, Figure 16b reveals the presence of imbedded particles and pullouts, also indicative of a drawn surface. Aside from these, the surface of the tubing was essentially featureless, exhibiting neither any grain boundary structure nor any unusual surface morphology. In contrast, the IN 600 thermowells removed from the pool-boiler exhibited dramatic changes in structure. Figures 17a and b show the surface of a thermowell that was located below the liquid level of the NaK. At low magnification, the surface striations apparent in Figure 16a are no longer visible nor are the areas of darker contrast associated with surface contamination. However, the grain boundary structure can be clearly seen, obvious evidence of intergranular attack. At high magnification, Figure 17b the nature of the grain boundary dissolution is apparent. The alloy immediately adjacent to each grain boundary has a faceted appearance indicated that there was preferential dissolution along certain crystallographic orientations. Figure 17b also reveals that the grain surfaces themselves exhibit similar faceting, indicating that the alloy as a whole was subject to crystallographically preferred dissolution. The response of the IN 600 was the same in the condenser and as such no additional microscopy is presented. Metallographic cross-sections of the NaK-exposed tubing were prepared and it was determined that the grain boundary dissolution extended approximately 1-2 grain diameters into the tubing sidewall. The behavior of IN 600 observed here was similar to that reported for another nickel-based alloy, IN718, exposed to NaK at temperatures between 677°C and 777°C.[17] In that study the alloy exhibited evidence of grain boundary attack after 1090 hours of exposure.

– leak site

The pool-boiler test was terminated after a small change in the characteristic temperature response was recorded.[2] It was determined that this change resulted from the loss of vacuum due to a very small leak. The recorded pressure rise was ≈ 10 torr. The source of this vacuum leak was identified during the course of this analysis. The leak occurred in one of the IN 600 thermowells used to record the temperature of the vessel sidewall in the condenser. In addition to being brazed to the endcap of the pool-boiler, this thermowell was brazed to the vessel sidewall in order to improve thermal coupling and insure continuous contact over the lifetime of the test. The rigid attachment of the thermowell at both ends gave rise to a mechanical fatigue profile induced by thermal cycling. Although the thermal expansion coefficients of Haynes 230 and IN 600 are quite similar [4, 18], the heating rate of the thermowell is likely to have been much more rapid because of its location within the vessel (and therefore the absence of any heat loss) and because of its considerably smaller mass than the pool-boiler vessel. It was this difference in heating rate rather than in thermal expansion coefficient that gave rise to the continuous thermo-mechanical fatigue cycle. The ensuing initiation and growth of a fatigue crack caused the loss of vacuum. Within the pool-boiler, the alloy was particularly sensitive to mechanical fatigue failure due to its susceptibility to grain boundary dissolution as illustrated above.

Figure 18a shows the actual location of the leak site immediately beyond the brazed end of the thermowell. The tube shows clear evidence of "necking" in a fashion similar to a conventional mechanical test specimen and confirms that there was a significant concentration of strain at the point of failure. This thermowell alloy may have been particularly sensitive to mechanical deformation if the brazing procedure annealed the tube, weakening it relative to the rest of the thermowell. The leak site is identified in Figure 18a by the arrow. The leak was located at the minimum diameter in the neck and initiated in the side of the tube opposite (facing) the pool-boiler sidewall. Figure 18b

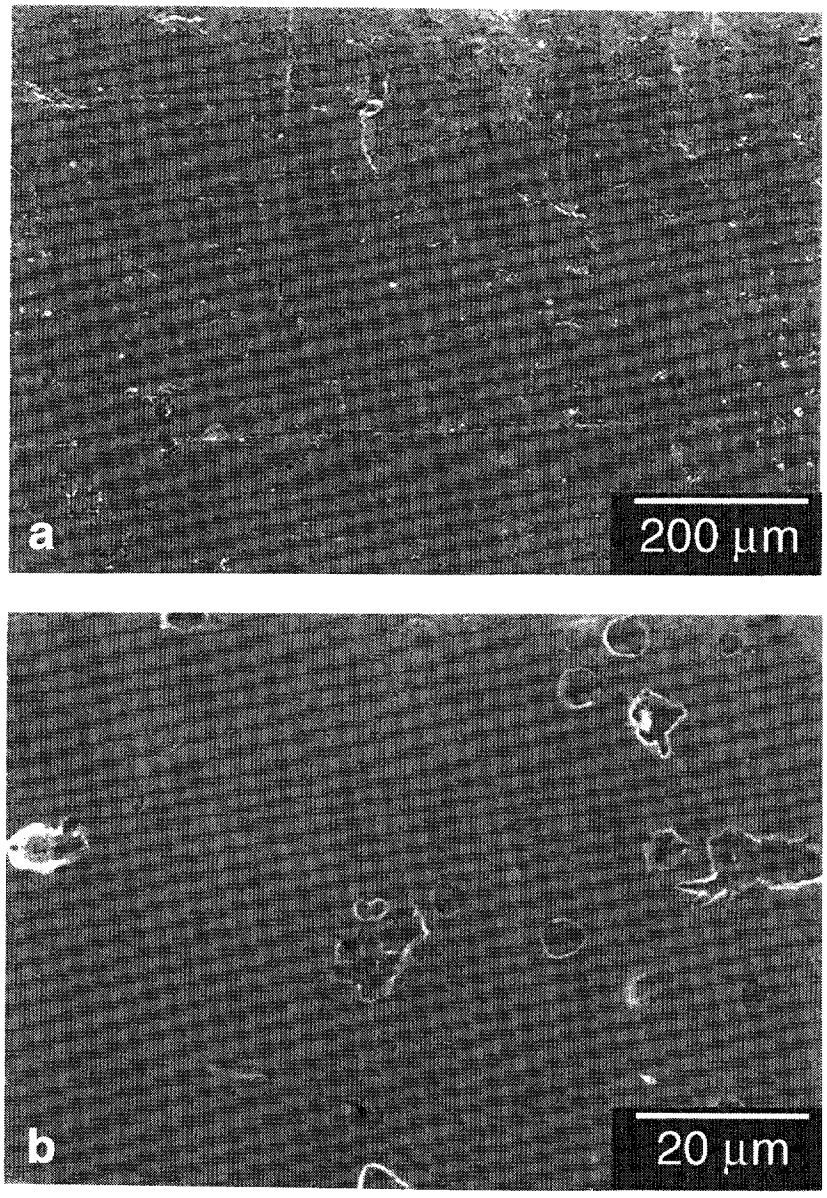

Figure 16. a) Scanning electron micrographs of the as-formed IN600 thermowell tubing. b) Imbedded particulates and pullouts are evident on the surface of the as-formed tubing.

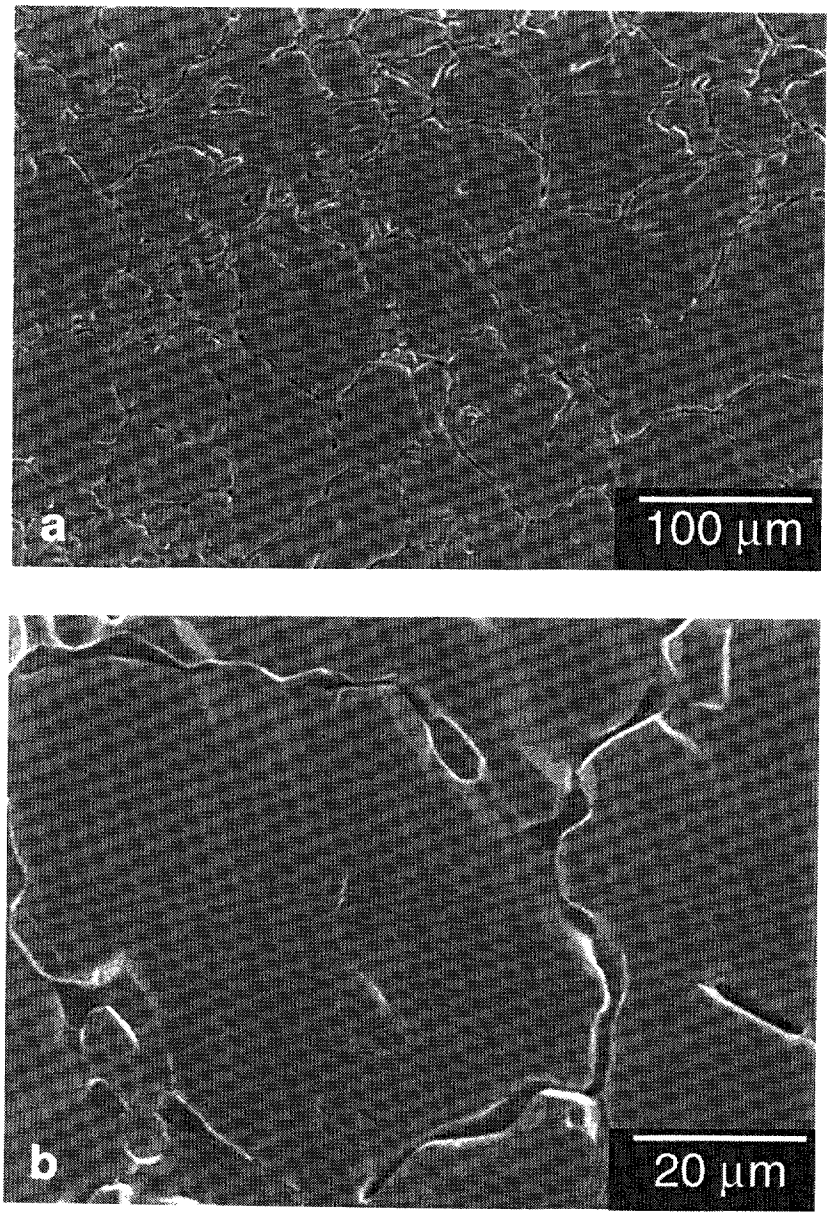

Figure 17. Surface of an IN600 thermowell that was located below the liquid level of the NaK. a) At low magnification, the grain boundary structure is clearly revealed as the result of grain boundary dissolution. b) Dissolved grain boundaries and grain surfaces have a faceted appearance indicated that there was preferential dissolution along certain crystallographic orientations.

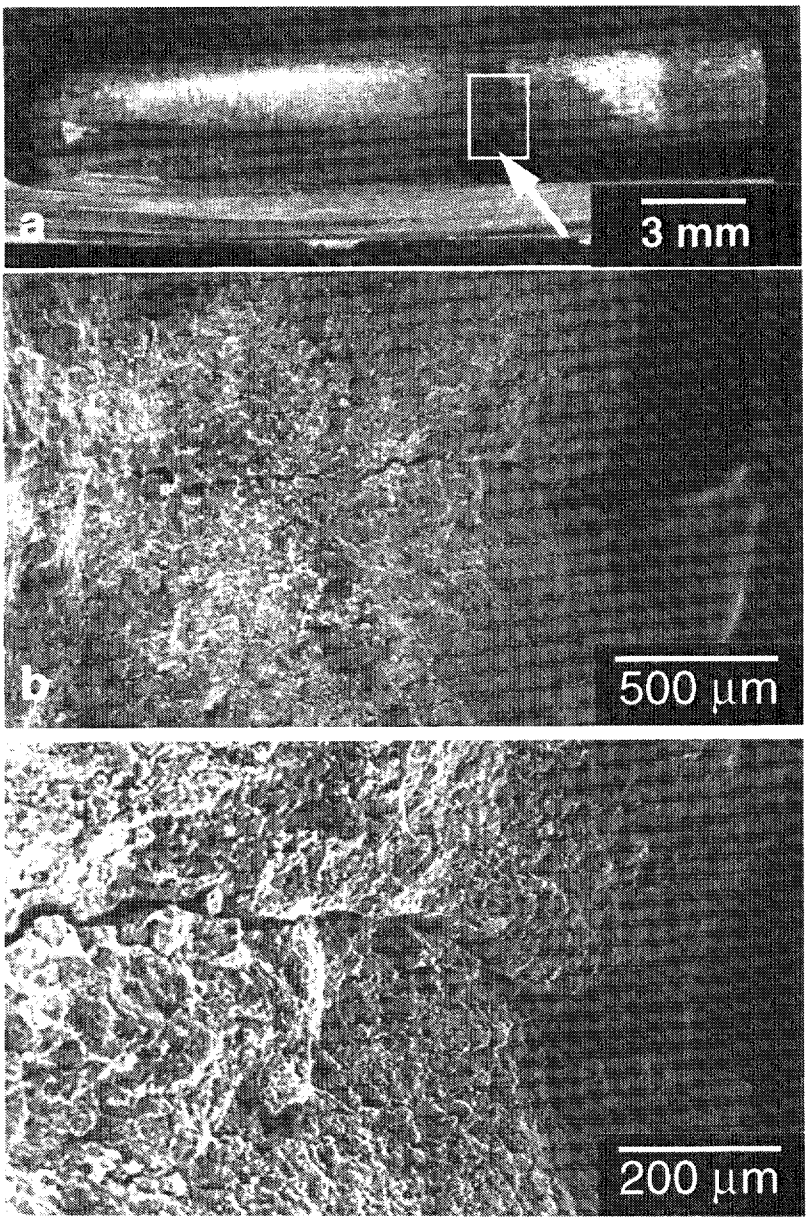

Figure 18. Scanning electron micrographs of the leak site in the IN600 thermowell. a) Leak is located at the arrow and runs vertically in the necked (boxed) regions of the tube. b,c) Higher magnification images are rotated 90° from that presented in (a). The crack extends nearly half way around the diameter of the tube.

and c are scanning electron micrographs of the section of the thermowell highlighted in Figure 18a. These micrographs show the sidewall of the thermowell ≈ 90° away from the initiation site of the crack. Note that images in Figure 18b and c are rotated relative to the image of the thermowell in Figure 18a for ease of presentation. Figure 18b shows that the crack was quite long, extending nearly half way around the diameter of the tube. Rigorous characterization of the fatigue crack (i.e., intergranular vs. transgranular) was not possible for several reasons. First, the crack experienced a tension-compression fatigue profile. The mechanical damage to the crack faces during each compressive loading would obscure their detailed structure. Second, as the NaK was exposed to air, sodium and potassium oxides would form locally. These oxides are quite reactive with respect to the alloying elements of IN 600 and can rapidly obliterate even more of the detailed structure of the leak site. Regardless of the precise details of the thermowell failure, the leak through the IN 600 tube is further reason to preclude its use in similar liquid metal environments. Other studies have reported similar grain-boundary corrosion of IN 600 exposed liquid potassium at 890°C after 500 hours that was especially pronounced at the liquid-vapor interface. [19]

Nickel

As with the IN 600, the nickel ribbon was not considered a critical material for pool-boiler technology. Its response to extended NaK exposure is presented because of what the results suggest about the suitability of alloys having high nickel content. The nickel ribbon immersed in the NaK exhibited evidence of catastrophic attack after 7500 hours at 750°C. SEM micrographs of the ribbon surface are shown in Figures 19a and b.
In Figure 19a, the grain boundary structure of the nickel is sharply delineated as the result of pitting and selective dissolution. Away from the grain boundaries there is additional pitting everywhere on the surface of the ribbon. The general faceted appearance of the grain boundary attack is similar to that shown in Figures 17a and b for the IN 600 thermowells. At higher magnification, Figure 19b shows the uniformity of these 5-10 μm diameter surface pits. It is clear from this micrograph that dissolution has occurred along preferred crystallographic planes giving rise to the sharply faceted surface features and angular pits.

The extent of damage and the depth of pitting is shown in Figures 20a, b and c which are scanning electron micrographs of a polished cross-section of the nickel ribbon.
Figure 20a reveals that the cavitation resulting from dissolution of nickel extended more than 30 μm below the ribbon surface. The faceting of the free surfaces of the nickel ribbon in Figure 19b is made more evident in Figure 20b. Figure 20c clearly shows that the dissolution is occuring along the grain boundaries of the nickel ribbon. The cavity microstructure is interconnected, allowing for the rapid dissolution of nickel from deep within the interior of the ribbon. EDS analysis revealed the presence of small concentrations (≤ 1 wt.%) of Cr, Fe and Zr in a surface layer several microns thick. The presence of these elements in the nickel ribbon arise from their dissolution in the NaK (Fe and Cr from the Haynes 230 vessel and IN 600 thermowells and the Zr from the oxygen getter) and subsequent deposition on and diffusion into the nickel foil. While the absolute amounts of these constituents were quite small, their presence was additional confirmation of the occurrence of mass transport within the pool-boiler.

BNi-3

– as-brazed

Figure 21a is an optical micrograph that shows the microstructure of a typical as-brazed joint between the Haynes 230 pool-boiler vessel to the Haynes 230 endcap. Within the interior of the braze some spherical porosity was occasionally noted (although not shown in this figure). This porosity is presumed to have formed during the brazing cycle due to entrapped gas. Figure 21b, also a higher magnification micrograph and reveals that the

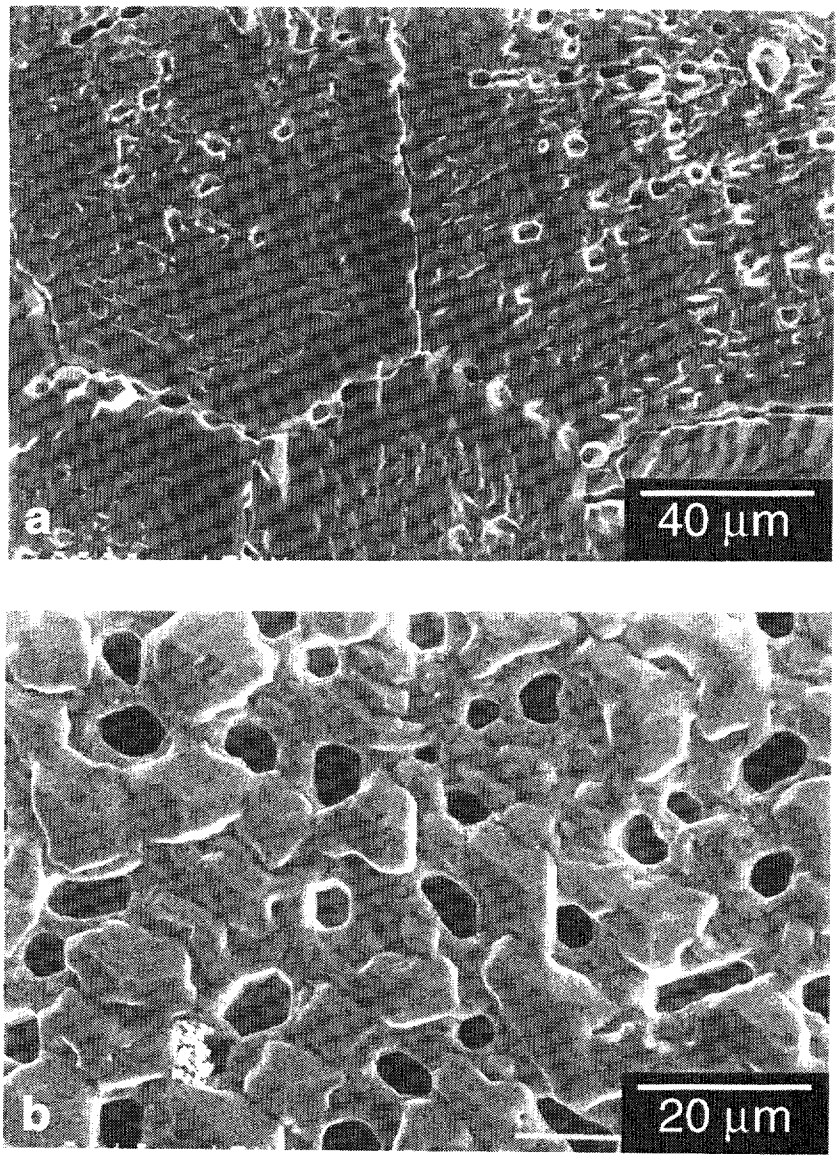

Figure 19. a) SEM micrograph of nickel ribbon immersed in the NaK exhibits evidence of catastrophic attack after 7500 hours at 750°C. The grain boundary structure of the nickel is revealed as the result of pitting and selective dissolution of the nickel near the boundaries, while away from the grain boundaries there is additional pitting. b) At higher magnification, it is clear that dissolution has occurred along preferred crystallographic planes giving rise to the sharply faceted surface features and angular pits.

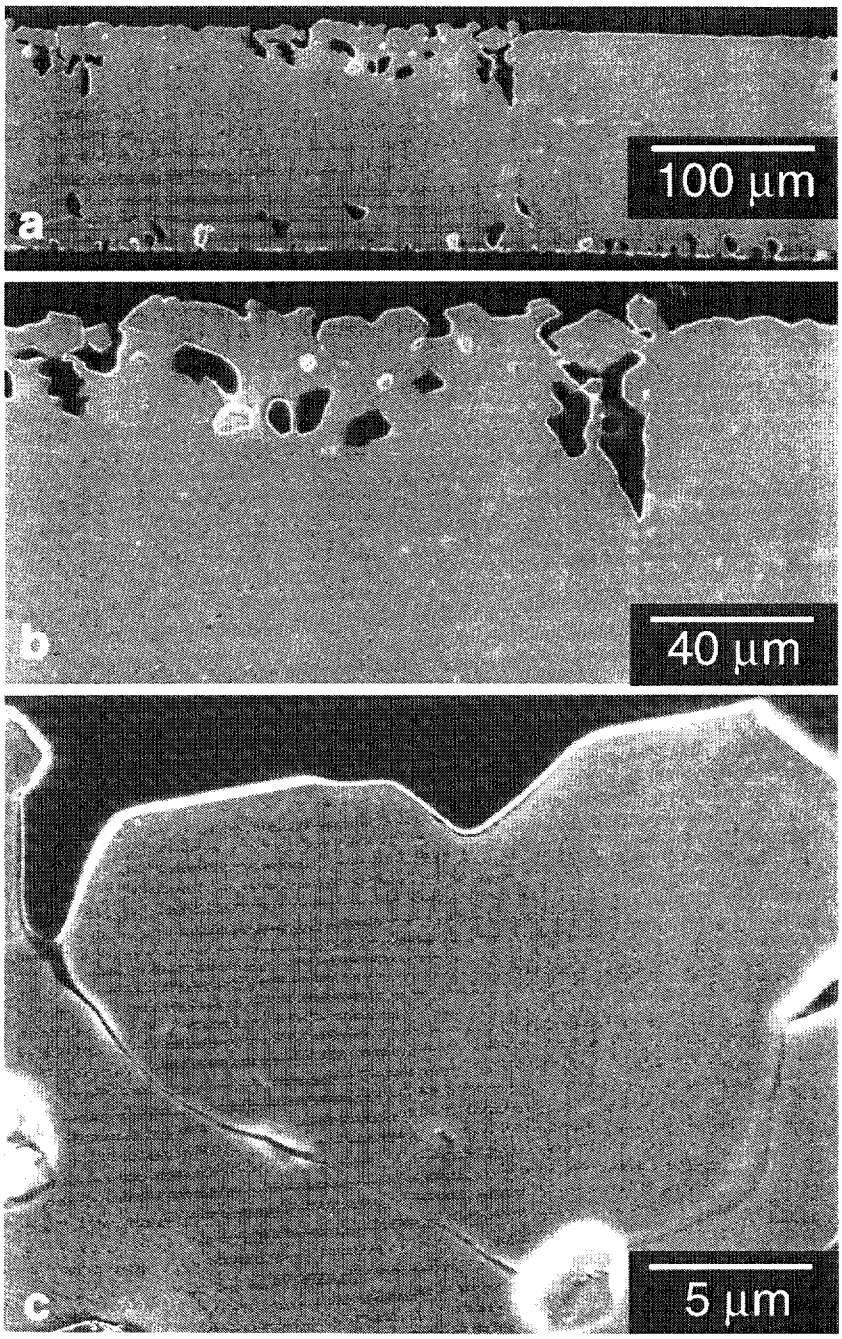

Figure 20. Scanning electron micrographs of a polished cross-section of NaK-exposed nickel ribbon. a) Cavitation extends more than 30µm below surface. b) Exposed surface exhibits facets suggesting crystallographic dissolution. c) Grain boundary dissolution is apparent at high magnification.

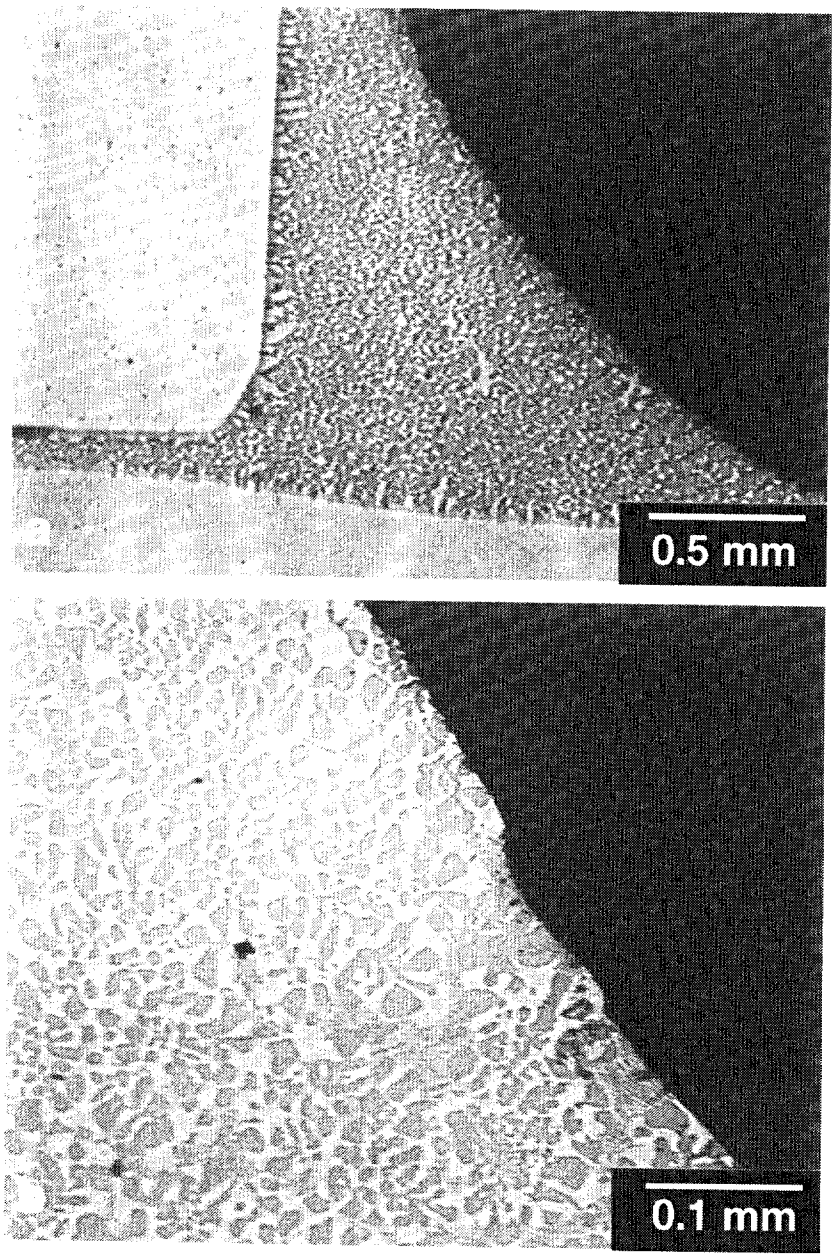

Figure 21. a) Optical micrograph of a typical as-brazed joint between pool boiler vessel and endcap. b) The bulk of the braze consists of a two-phase structure. The lighter phase is nickel - boron. The darker regions are nickel - silicon. These two phases exist in nearly equal proportions.

bulk of the braze consisted of a two-phase structure. EDS analysis was used to determine the composition of these two regions. The results reveal that the lighter phase shown in Figure 21b was a composed of ≈ 94 wt.% nickel and ≈ 5.5 wt.% boron while the darker regions were composed of ≈ 88 wt.% Ni and ≈ 11 wt.% silicon. Both phases contained between 0.5 and 1.0 wt.% chromium. These two phases existed in nearly equal proportions and therefore the elemental analyses are consistent with the overall composition of the braze alloy presented in Table I. Backscatter electron imaging revealed that the silicon-rich phase (either as-brazed or NaK-exposed) was, in fact, composed of a finer structure containing regions of greater and lesser silicon (see Figure 22). At high magnification the interface between the braze and the Haynes 230 showed evidence of other phases resulting from the interdiffusion of the BNi-3 and Haynes 230 constituents. The formation of such structures in brazed joints is common and is minimized by holding temperature and time to the minimum necessary to achieve a sound joint.[20]

– NaK-exposed brazes

The response of the BNi-3 brazes in the boiler and in the condenser section of the device was identical. The exposed brazes showed evidence of both NaK-induced dissolution and thermal aging effects. Figure 22 is a BSE scanning electron micrograph of a cross-section of a braze exposed to NaK liquid. As with the SEI images in Figures 21a and b, the lighter regions in the micrograph are composed of a nickel-boron phase while the generally darker regions are a nickel-silicon phase. The complex structure of the Ni-Si phase mentioned in the previous paragraph is apparent in Figure 22 and arises from the partitioning of the silicon into regions of relatively greater and lesser concentrations. The phase diagram for Ni-Si suggests that these two regions would consist of a nearly pure nickel phase and a phase consisting of ≈ 86% wt.% Ni and 14 wt.% Si.[21]

The principal effect of long-term exposure to NaK can be seen in Figure 22 which reveals that there was dissolution of braze alloy at the NaK-exposed surface. It is apparent that most of the loss was confined to the darker, Ni-Si phase. This dissolution was confined to the near-surface of the braze as there was no evidence of the formation of internal porosity beyond that which was observed in the unexposed brazes. The preferential attack of the Ni-Si phase arises from its microstructure – specifically its partitioning into regions of nearly pure nickel and nickel-silicon alloy. The regions of nearly pure nickel within the Ni-Si phase are as susceptible to attack as was the nickel ribbon described in the previous section. It is through these regions of nickel that NaK aggressively attacks the braze.

The nickel-boron phase within the braze also showed evidence of a small amount of attack. The NaK-exposed surfaces of the Ni-B phase regions have angular edges, much like the NaK-exposed surface features of the nickel ribbon described above. This contrasts to the rounded edges of the phase boundaries within the interior of the braze. As before, such features arise as the result of preferential dissolution along certain crystallographic planes.

EDS analysis of the cross-section shown in Figure 22 revealed that chromium was present in a narrow band extending from the NaK-exposed surface to a depth of approximately 20 μm. The only source of chromium in the system is that which was dissolved into the NaK from the Haynes 230 vessel or the IN 600 thermowells. While this observation is only of incidental importance in relation to the interaction of the braze alloy with NaK, it is noteworthy in that it is yet another instance of mass transport and deposition identified in this pool-boiler system.

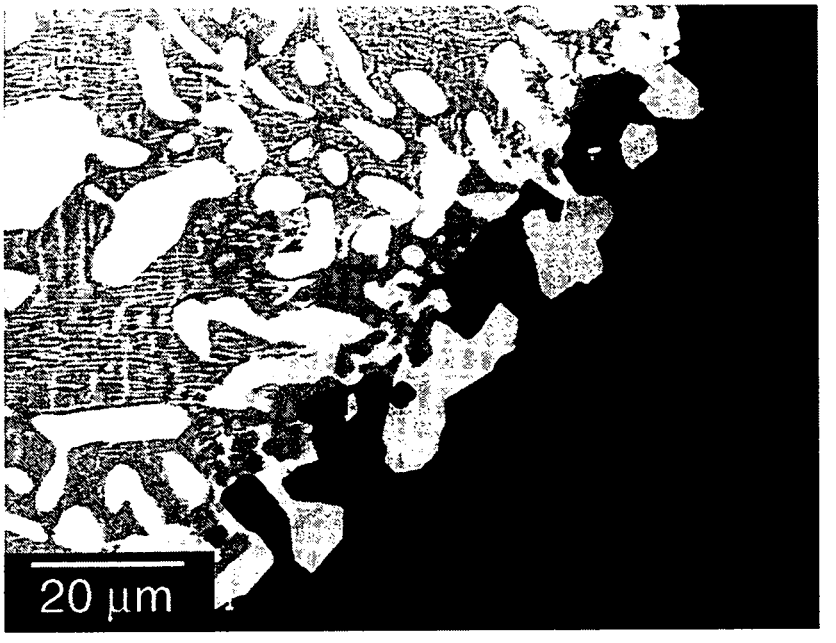

Figure 22. Backscatter electron image reveals loss of braze alloy at NaK-exposed surface. The darker regions in the micrograph are composed of a nickel-boron phase while the generally lighter regions are a nickel-silicon phase. The complex structure of the Ni-Si phase arises from the partitioning of the silicon into regions of relatively greater and lesser concentrations.

Elemental trace analyses were performed across the braze/Haynes interface for both as-brazed and NaK-exposed joints using WDS (wavelength dispersive spectroscopy) analysis. Figure 23a shows the results for the as-brazed specimen. For the sake of clarity, only the major elemental constituents are shown, as is the approximate position of the interface. Data was collected at 1 μm intervals (symbols for every data point are not shown, also for the sake of clarity). The brazing procedure alone induced only a very small amount of interdiffusion across the interface. This resulted in a very narrow interdiffusion zone that extended about 3-4 μm on either side of the interface. Nickel and silicon diffused from the BNi-3 braze alloy into the Haynes 230 while tungsten and chromium diffused in the reverse direction. Away from the interface, the concentrations of these elements approach those of the baseline specifications for the respective alloys. Interdiffusion of boron was not evident in this analysis.

Within the pool-boiler, the interface between the braze and the Haynes 230 exhibited evidence of thermal aging effects. The resulting microstructure was quite complex and an exhaustive analysis of all of the microstructural changes was beyond the scope of the current work. However, it is useful to review the two principal effects: (1) the broadening of the interdiffusion zones on either side of the braze/Haynes interface and (2) the formation of low-Z intragranular and grain boundary structures in the Haynes to a depth of several grain diameters from the interface.

Figure 23b, an elemental trace analysis, illustrates the first effect. After the prolonged exposure, the interdiffusion zone was much broader than that shown in Figure 23a. The diffusion of silicon and boron into the Haynes 230 could be of particular concern if it were to result in the formation of silicides and borides, thus depleting the matrix of alloying constituents or promoting the formation of brittle grain boundary phases. In the present instance though, we have no evidence (e.g. cracking or porosity) of the braze structures or of the vessel alloy being compromised in any way by such processes.

Figures 24a and b are backscatter electron images of the Haynes 230 endcap near a BNi-3 braze from the pool-boiler and are representative of the low-Z grain boundary structures that form during long-term, high temperature exposure. The specimen shown in these micrographs was polished and unetched. Contrast therefore results only from compositional variations between regions within the material. Because it has a net lower Z than the Haynes alloy, the braze appears as the very dark region to the right and to the bottom of the micrograph in Figure 24a. The grain boundaries in the Haynes near the braze (within 100-200 μm of the interface) appear much darker than boundaries further away and are evidence that lighter elements from the braze alloy, either silicon or boron, have diffused into the Haynes after long times at temperature and have segregated to the grain boundaries. The extent of segregation is seen more clearly in Figure 24b, a higher magnification image of the highlighted region in Figure 24a.

Figure 25a is a backscatter electron image of the braze/Haynes 230 interface after 7500 hours at temperature. As in the previous instance, the specimen shown in this figure was examined in the polished and unetched condition, so that contrast in the micrograph results only from compositional variations between regions within the sample. Figure 25a reveals both the dark grain boundaries extending to a depth of 100-200 μm illustrated in the previous figure and the dark needle-like intragranular features mentioned above. X-ray mapping of this region was performed in order to identify which elemental species were segregating to these dark features. Such maps for boron and chromium are shown in Figures 25b and c. These maps reveal that the dark intragranular needles, as well as the darkened grain boundaries, contained elevated levels of boron and chromium relative to the surrounding Haynes matrix. No preferential segregation of silicon was observed. In addition, the braze alloy adjacent the interface exhibits a 40 μm wide band

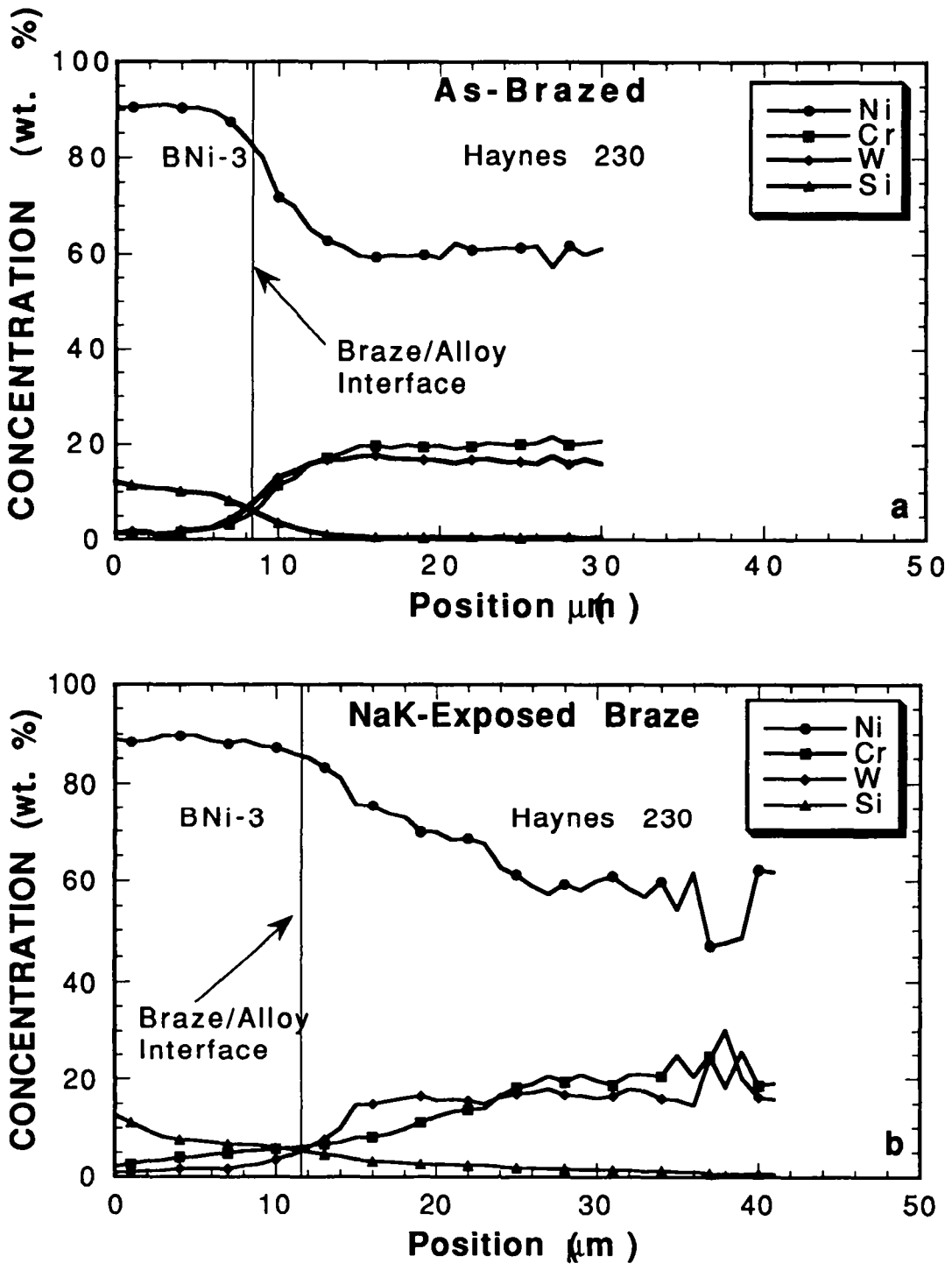

Figure 23 a) EDS analysis of principal alloying constituents at as-received braze/Haynes interface. b) Similar elemental analysis across braze/Haynes interface from pool-boiler.

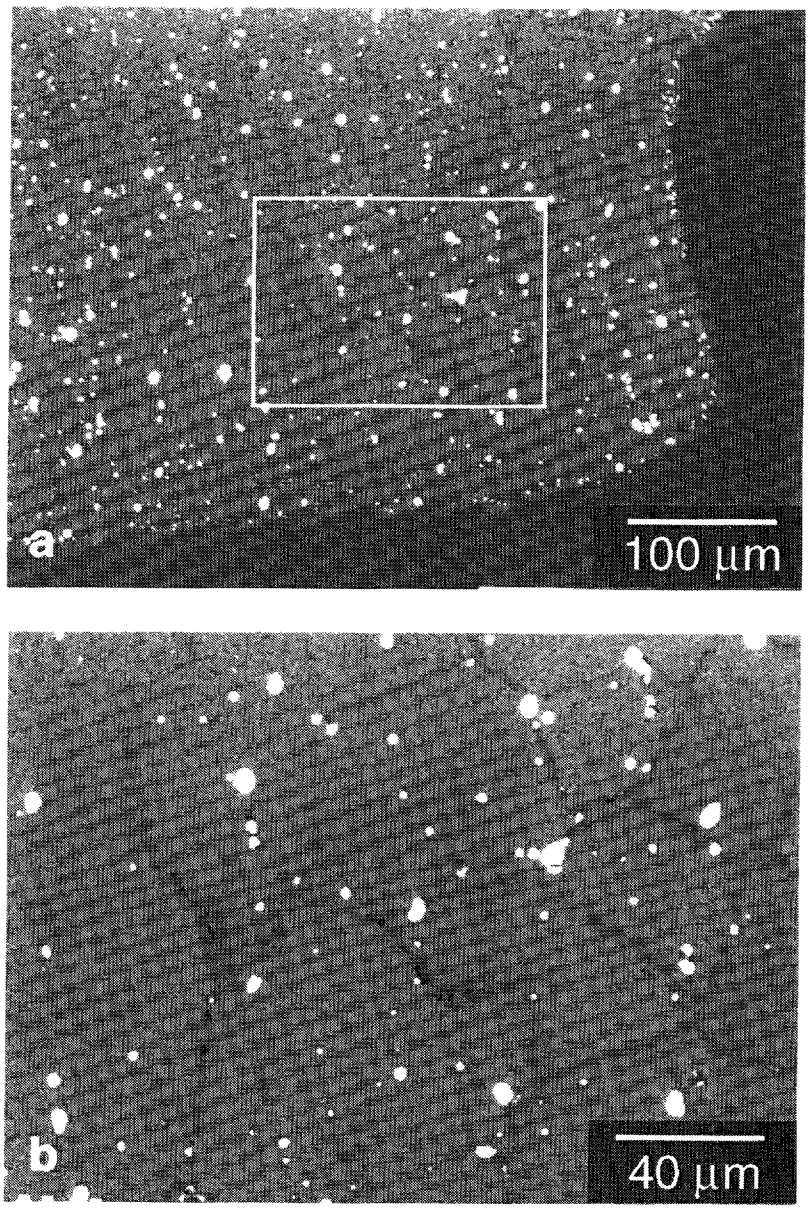

Figure 24. a) Backscatter electron images of the Haynes 230 endcap near a BNi-3 braze from the pool boiler showing low-Z grain boundary structures. b) The extent of segregation is seen more clearly in this higher magnification image of the highlighted region in (a).

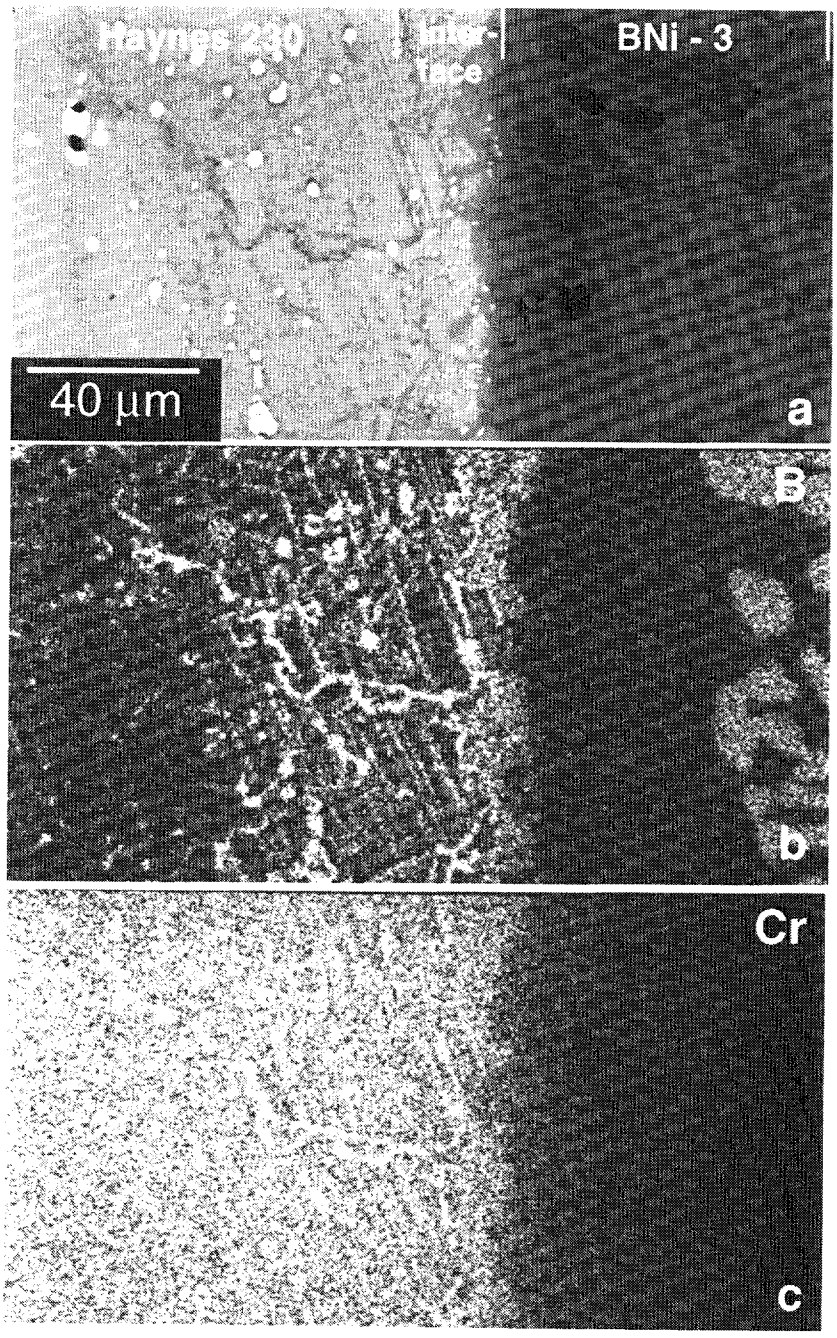

Figure 25. a) Backscatter electron image of the braze/Haynes 230 interface after 7500 hours at temperature. b) Boron X-ray map of the region shown in (a). c) Chromium X-ray map of the same region.

that is depleted in boron. This boron depleted region is the source of the boron found in the Haynes.

Not withstanding these various microstructural and composition changes in the vicinity of the braze/Haynes interface, the performance the brazes and the vessel alloy near the brazes was unaffected. No cracking or porosity in the Haynes 230 or the brazes was observed nor was there any evidenced of enhanced dissolution in the pool-boiler vessel near the endcap brazes.

Zirconium getter

The zirconium getter exhibited profound changes after 7500 hr of pool-boiler operation. Whereas the starting material had the spring-like characteristics of a thin cold-worked metal sheet and had a mirror-like finish, the getter removed from the pool-boiler was brittle and had a matte finish. Indeed, the getter fractured into about 10 large fragments upon removal from the vessel. X-ray diffraction confirmed the presence of elemental zirconium, thereby ensuring that adequate gettering capacity existed throughout the test. The X-ray diffraction spectra also indicated the presence of numerous minor phases which could not be conclusively identified.

To further investigate the compositional changes in the getter, sections of the as-received metal sheet and NaK-exposed material were dissolved in nitric acid and the metallic content was determined quantitatively by inductively-coupled plasma atomic emission spectroscopy (ICP-AES). The alloying elements detected by this procedure are shown in Table IV. Both nickel and chromium were found in the aged getter at concentrations that far exceed those in the as-received sheet. The obvious source of these elements are those materials used in the test assembly that showed evidence of dissolution. However, neither Ni or Cr were present in sufficient quantity to account for all the material dissolved from the pool-boiler. Since the Zr getter was only a minor sink for these elements, it is unlikely that its presence enhanced the dissolution of Ni and Cr from elsewhere in the pool-boiler.

The origin of physical changes in the getter is difficult to determine unambiguously. Since zirconium can form intermetallic compounds with both nickel and chromium, it is possible that these compounds may be the source of the observed embrittlement. Alternatively, the embrittlement could be the result of the formation of zirconium oxide due to the thermowell leak.

TABLE IV: Metallic constituents of zirconium getter (wt. ppm)

Element	As-received	Pool-boiler
Nickel	19	35000
Chromium	65	4150
Iron	305	260
Silicon	7	72
Tungsten	14	12
Zirconium	bal	bal

NaK analysis
After the pool-boiler had cooled to room temperature, several attempts were made to analyze the NaK for dissolved metals. Both ICP/AES and ICP/MS (mass spectroscopy) were used to identify the presence of soluble zirconium (from the getter), nickel, chromium and the other principal alloying elements of Haynes 230 and IN 600. Neither of the analytical techniques were successful in unambiguously identifying elevated concentrations of these elements in the NaK from the pool-boiler relative to archived samples of the as-received NaK. These results are not surprising as the solubility of the major alloying constituents in sodium and potassium are very temperature dependent (see Figure 7). Indeed, the metals of interest are nearly insoluble at room temperature. As similar behavior can be expected for NaK, the absence of the soluble alloy constituents in the NaK is not inconsistent with the observations of alloy dissolution and elemental deposition as described in various sections of this report.

IV. SUMMARY

Haynes Alloy 230
The alloy used to construct the pool-boiler vessel, Haynes 230, exhibited evidence of some interactions with the NaK environment. Examination of samples removed from the boiler and condenser walls after 7500 hours at a 750°C indicated that a surface layer several microns thick was affected by the liquid metal. In general, the interaction appeared to arise from preferential dissolution of nickel and chromium from the alloy matrix exposing the pre-existing tungsten-rich precipitate microstructure. While the precise details of these interactions varied with location in the boiler, the minimal dissolution observed, even in the worst cases, suggests that this alloy is suitable for use in further development studies and for longer periods of operation. The corrosion behavior of the NaK-exposed autogenous welds was essentially identical to that of the parent alloy. Air-side corrosion of the pool-boiler vessel parent metal and autogenous welds was inconsequential.

The implications of the changes in mechanical properties are more difficult to assess. The loss of ductility in itself is not sufficient to disqualify the alloy for use in pool boiler applications. However, if longer-term exposures result in further degradation of mechanical properties, the useful service life of a commercial structure may be constrained.

Enhanced boiling surface
The stainless steel enhanced boiling surface performed well. Only the most minimal dissolution of the 304L SS powder was observed. There was no evidence of any cracking or spalling due to the thermal mismatch between the Haynes 230 vessel and the brazed structure. The structure exhibited no evidence of sintering or further densification after prolonged times at temperature.

IN 600, nickel
Other nickel-based materials exhibited poor compatibility with this liquid metal environment. IN 600 suffered substantial intergranular attack, while the nickel ribbon experienced extensive dissolution, resulting in the formation of large internal cavities. Although the failure of an IN 600 thermowell resulted in the termination of the experiment after ≈ 7500 hours, its use in pool-boiler designs is not essential. Other alloys more suitable for use in this application should be substituted in future experiments.

Brazes

The BNi-3 structural brazes performed well over the duration of the experiment. While the surfaces exposed to NaK or its vapor show clear evidence of attack, the metal loss appeared to be relatively small. The changes in interface structure and composition resulting from thermal aging give rise to concerns regarding loss of ductility and the response such joints to thermo-mechanical fatigue. It is difficult to assess the potential performance of this alloy in longer-term systems since the impact of the chemical attack and the thermal aging effects will depend entirely on the design and geometry of a brazed joint.

Zr getter

The getter remained active throughout the test. However, the tendency of the getter to interact with constituents of the structural alloys complicates the ability to extrapolate its effectiveness to longer operating times. The obvious physical changes in the getter appear to have resulted from the uptake of nickel dissolved from the nickel-bearing alloys used in the test assembly or from oxidation due to the thermowell leak at the end of the experiment.

V. REFERENCES

1. W. B. Stine and R. B. Diver, "A Compendium of Solar Dish/ Stirling Technology", SAND93-7026, Sandia National Laboratories, Albuquerque, NM. 87185, January 1994.

2. C. E. Andraka, J. B. Moreno, T. A. Moss, S. A. Jones, NaK Pool-Boiler Solar Receiver Durability Bench Test, Vol 1: Test Design and Results, SAND94-1538, Sandia National Laboratories, Albuquerque, NM., 87185, In press.

3. P. F. Tortorelli, in Fundamentals of High Temperature Corrosion in Liquid Metals, Metals Handbook, Vol. 13, pp. 56-60, 1987, ASM Int., Materials Park, OH.

4. Haynes Alloy 230, Haynes International, Inc., Kokomo IN, 46904.

5. NICROBRAZ® Technical Data Sheet, D2.1.1 REV. P, Wall Colmonoy Corp., Madison Heights, MI, 48071.

6. J. B. Moreno, and T. A. Moss , "Bench Scale Screening Tests for a Boiling Sodium-Potassium Alloy Solar Receiver", SAND92-2253, Sandia National Laboratories, Albuquerque, NM., 87185, June 1993.

7. R. M. Singer and R. E. Holtz, "The Vaporization of Superheated Sodium in a Vertical Channel", Trans. ASME., 94, Series C, p. 300, 1972.

8. C. E. Andraka, S. A. Jones, J. B. Moreno, and T. A. Moss, "NaK Pool-Boiler Bench Scale Receiver Durability Test: Test Design and Initial Results", Proceedings of the 28th Intersociety Energy Conversion Engineering Conference, August 1993.

9. Private communication, D. Klarstrom, Haynes International, Inc., Kokomo, IN, 46904.

10. T. Claar, "Solubilities of Metallic Elements in Liquid Sodium", Reactor Tech., 13 (2), p.124, 1970.

11. J . R. Weeks and H. S. Isaacs, in Advances in Corrosion Science and Technology, M. G. Fontana and R. W. Staehle, Editors, Plenum, Vol. 3, p. 10, 1973.

12. J. H. Swisher, "Solubility of Iron, Nickel and Cobalt in Liquid Potassium and Effect of Oxygen Gettering Agents", NASA Lewis Research Center, NASA TN-D-2734, March 1965.

13. S. Stecura, in Corrosion by Liquid Metals, J. E. Draley and J. R. Weeks, Editors, Plenum Press, p. 601, 1970.

14. Sodium-NaK Engineering Handbook, Vol. 5, p. 244, O. J. Foust, Editor, Gordon and Breach Publishing, 1972.

15. D. L. Klarstrom, "The Thermal Stability of a Ni-Cr-W-Mo Alloy", Proceedings of Corrosion 94, Paper #407, NACE, 1994.

16. L. L. Shreir, R. A. Jarman and G. T. Burstein, Corrosion - Metal/Environment

Reactions, Third edition, Vol. 1, p. 2:120, Butterworths, 1994.

17. S. E. Walak, M.J. Cronin and T. Grobstein, "Heat Pipe Fatigue Test Specimen Metallurgical Analysis", NASA Contractor Report 189120, MTI Report 91TR56, January 1992.

18. Inconel Alloy 600 , Inco Alloys International, Huntington,WV, 25720.

19. J. H. Stang, E. M. Simons, E. A. DeMastry and J. M. Genco, "Compatibility of Liquid and Vapor Alkali Metals with Construction Materials", Battelle Columbus Laboratories, DMIC Report 227, April 1966.

20. Brazing Manual, 3rd Edition, American Welding Society, Miami, FL, 1976.

21. T. B. Massalski, et al., Binary Alloy Phase Diagrams, Second Edition, ASM Int. Materials Park, OH, 1990.

UNLIMITED DISTRIBUTON:

U.S. Department of Energy (5)
Attn: G. Burch
S. Gronich
Forrestal Building
Code EE-132
1000 Independence Avenue, SW
Washington, DC 20585

U.S. Department of Energy (2)
Attn: R. Annan
Forrestal Building
Code EE-13
1000 Independence Avenue, SW
Washington, DC 20585

U.S. Department of Energy (2)
Attn: G. Tennyson
N. Lackey
Albuquerque Operations Office
P.O. Box 5400
Albuquerque, NM 87115

U.S. Department of Energy
Attn: R. Hughey
San Francisco Operations Office
1333 Broadway
Oakland, CA 94612

Arizona Public Sevice Company
Attn: S. McLellan
P.O. Box 53999, MS 1424
Phoenix, AZ 85072-3999

Arizona Solar Energy Office
Attn: F. Mancini
Dept. of Commerce
3800 N. Central
Phoenix, AZ 85012

Australian National University
Attn: S. Kaneff
Department of Engineering Physics
P. O. Box 4
Canberra ACT 2600 AUSTRALIA

Battelle Pacific Northwest Lab (2)
Attn: D. Brown
P.O. Box 999
Richland, WA 99352

California Polytechnic University
Attn: W. Stine
Dept. of Mechanical Engineering
3801 West Temple Avenue
Pomona, CA 91768-406

Clever Fellows
Innovation Consortium, Inc.
Attn: J. A. Corey, P.E.
R.D. 1, Box 410, River Road
Melrose, NY 12121

Cummins Power Generation
Attn: J. Davis
MC 60125
P. O. Box 3005
Columbus, IN 47202-3005

Cummins Power Generation (2)
Attn: I. Kubo
MC 50179
P. O. Box 3005
Columbus, IN 47202-3005

Cummins Power Generation South
Attn: M. McGlaun
150 Tannehill Drive
Abilene, TX 79602

DLR
Attn: R. Buck
Pfaffenwaldring 38-40
7000 Stuttgart 80 GERMANY

Dynatherm Corporation
Attn: David Wolf
1 Beaver Court
P.O. Box 398
Cockeysville, MD 21030

Electric Power Research Institute
Attn: J. Schaeffer
P.O. Box 10412
Palo Alto, CA 94303

Energy Research Centre (2)
Attn: K. Inall
R. S. Phy. Sc.
Australian National University
Canberra ACT 2601 AUSTRIALIA

Energy Technology Engr. Center (2)
Attn: W. Bigelow
R. LeChevalier
Rockwell International Corp.
P. O. Box 1449
Canoga Park, CA 91304

Failure Analysis Associates Inc.
Attn: Larry Eiselstein
149 Commonwealth Dr.
Menlo Park, CA 94025

Florida Solar Energy Center
Attn: Library
300 State Road, Suite 401
Cape Canaveral, FL 32920

Georgia Power
Attn: W. King
7 Solar Circle
Shenandoah, GA 30265

Institute of Gas Technology
Attn: Library
34245 State Street
Chicago, IL 60616

Jet Propulsion Laboratory
Attn: M. Alper
4800 Oak Grove Drive
Pasadena, CA 91109

Lawrence Berkeley Laboratory
Attn: A. Hunt
MS 90-2024
One Cyclotron Road
Berkeley, CA 94720

Los Alamos National Laboratory
Attn: M. Merrigan
MS-E13
Los Alamos, NM 87545

McDonnell-Douglas Astronautics Co. (3)
Attn: R. L. Gervais,
J. Rogan,
D. Steinmeyer
5301 Bolsa Avenue
Huntington Beach, CA 92647

Mechanical Technology, Inc. (3)
Attn: G. Dochat
J. Wagner
M. Cronin
968 Albany Shaker Road
Latham, NY 12110

NASA Lewis Research Center (4)
Attn: R. Shaltens
J. Schrieber
21000 Brook Park Road
Cleveland, OH 44135

National Renewable Energy Lab(6)
Attn: M. Bohn
G. Jorgensen
A. Lewandowski
L. M. Murphy
T. Wendelin
T. Williams
1617 Cole Boulevard
Golden, CO 80401

Northern Research and Eng. Corp.
Attn: J. Kesseli
39 Olympia Avenue
Woburn, MA 01801-2073

Pacific Gas and Electric Company
Attn: G. Braun
3400 Crow Canyon Road
San Ramon, CA 94583

Pacific Power
Attn: P. Lynch
Park and Elizabeth Streets
GPO Box 5257, Sydney
New South Wales 2001
AUSTRALIA

Power Kinetics, Inc. (2)
Attn: W. E. Rogers
415 River Street
Troy, NY 12180-2822

Research International
Attn: E. Saaski
18706 142nd Avenue NE
Woodinville, WA 98072

Schlaich, Bergermann & Partner
Attn: W. Schiel
Hohenzollernstr. 1
D - 7000 Stuttgart 1 GERMANY

Science Applications International Corp.
Attn: K. Beninga
15000 W 6th Avenue Suite 202
Golden, CO 80401

Science Applications International Corp.
Attn: B. Butler
Mail Stop 32
10260 Campus Point Court
San Diego, CA 92121

Solar Energy Industries Assoc. (2)
Attn: K. Sheinkopf
S. Sklar
777 North Capitol St. NE Suite 805
Washington, D.C. 20002-4226

Solar Kinetics, Inc. (2)
Attn: J. A. Hutchison
P. Schertz
P.O. Box 540636
Dallas, TX 75354-0636

Stirling Technology Company (2)
Attn: M. A. White
2952 George Washington Way
Richland, WA 99352

Stirling Thermal Motors (2)
Attn: Lennart Johansson
275 Metty Drive
Ann Arbor, MI 48103

Stirling Machine World
Attn: B. Ross
1823 Hummingbird Court
West Richland, WA 99352-9542

Sunpower, Inc.
Attn: W. Beale
6 Byard Street
Athens, OH 45701

Thermacore, Inc. (2)
Attn: D. Ernst
780 Eden Road
Lancaster, PA 17601

University of Houston (2)
Attn: J. Richardson
Solar Energy Laboratory
4800 Calhoun
Houston, TX 77704

University of Minnesota (2)
Attn: E. A. Fletcher
Dept. of Mechanical Engineering
111 Church St., SE
Minneapolis, MN 55455

MS 0835 D. R. Adkins, 1513
MS 0835 R. D. Skocypec, 1513
MS 0724 D. L. Hartley, 6000
MS 0735 D. E. Arvizu, 6200
MS 0704 P. C. Klimas, 6200
MS 1127 J. M. Chavez, 6215
MS 1127 P. G. Cordeiro, 6215
MS 1127 V. E. Dudley, 6215
MS 1127 A. R. Mahoney, 6215
MS 1127 K. S. Rawlinson, 6215
MS 0703 C. E. Tyner, 6216
MS 0703 C. E. Andraka, 6216 (5)
MS 0703 R. B. Diver, 6216
MS 0703 D. R. Gallup, 6216
MS 0703 T. R. Mancini, 6216
MS 0703 D. F. Menicucci, 6216
MS 0703 J. B. Moreno, 6216 (5)
MS 0703 T. A. Moss, 6216

MS 9001 J. C. Crawford, 8000
MS 9006 Attn: E. E. Ives, 5200
MS 9005 J. B. Wright, 5300
MS 9004 M. E. John, 8100
MS 9037 R. J. Detry, 8200
MS 9054 W. J. McLean, 8300
MS 9105 L. A. Hiles, 8400
MS 9002 P. N. Smith, 8500
MS 9901 L. A. West, 8600
MS 9108 M. Dyer, 8800
MS 9003 D. L. Crawford, 8900
MS 9401 R. C. Wayne, 8700
MS 9042 Attn: G. A. Benedetti, 8741
MS 9043 P. E. Nielan, 8742
MS 9043 M. L. Callabresi, 8743
MS 9042 R. J. Kee, 8745
MS 9044 W. A. Kawahara, 8746
MS 9405 D. L. Lindner, 5404
MS 9402 J. E. Costa, 8711
MS 9403 M. I. Baskes, 8712
MS 9404 J. C. F. Wang, 8713
MS 9404 E. Soria, 8713
MS 9402 M. W. Perra, 8714
MS 9402 S. H. Goods, 8714 (5)
MS 9402 G. J. Thomas, 8715
MS 9402 B. F. Bernal, 8715
MS 9402 C. Rood, 8715
MS 9402 A. D. Gardea, 8715
MS 9402 N. Y. C. Yang, 8715

MS 9404 J. M. Hruby, 8716
MS 9404 R. W. Bradshaw, 8716 (5)

MS9022 Publications to OSTI, 8533-1 (10)
MS9022 Mail Team Distribution, 8533-1/Technical Library, MS0899
MS0899 Technical Library Department, 13414 (4)
MS9018 Central Technical Files, 8523-2 (3)